

Dear editor,

The authors would like to thank you for reviewing this manuscript and applaud your attention to detail.

E1) In the spirit of one of the comments by reviewer #1 I would like to see the term "uncertainty quantification" replaced by "uncertainty assessment" wherever it appears.

A1) This change was made throughout the manuscript.

E2) Figure 1 has been changed quite substantially. Now it is not really clear why the upper part of the new version is faded out. Is this the part that will be treated in the follow-on paper? Please clarify (in the figure caption).

A2) The figure caption now reads: "Follow-on work will describe how observation can be post-processed and resampled to reduce the scale gap before model evaluation can be performed."

E3) Figure 2, caption: change b₂₋₄ into b₁₋₄ (first line).

A3) Great catch by the editor. The correction was made.

E4) 1st par. of section 3: "radiative scattering transfer" is a bad expression. I think "radiative transfer" suffices, since this expression includes scattering. If you deem the process of scattering should be emphasized here, then change to something like "radiative transfer, in particular scattering". The expression occurs twice and should be changed.

A4) Great suggestion. The expression "radiative scattering transfer" was changed to "radiative transfer" throughout the manuscript.

E5) 1st par of 3.1: "cloud particles backscatter THIS TYPE OF RADIATION the most". I don't know what this type of radiation is. Please reformulate.

A5) The expression was reformulated: "At a lidar wavelength of 532 nm, backscattered power is proportional to total particle cross section per unit volume. Owing to their high number concentrations, despite their small size, cloud particles backscatter radiation of this wavelength the most."

E6) Table 1, green column: I don't understand what "see questionable row" means, in particular since the row labelled "questionable" is empty in the green column.

A6) The expression "see questionable row" was replaced by: "Approximately equal to sum of questionable row: ($\sim 5.2 \pm 0.9$)".

E7) Lines 254-256 is almost exactly repeated in 276-278; the word "is" is missing in 255. Please correct.

A7) Great catch by the editor. This oversight was corrected.

E8) Eq. 29: Check the units. lhs has m/s, but rhs has $(m/2)^2$.

A8) The editor is correct, for consistency with the units mentioned in the text a square root was added to Eq. 29.

E9) line 880: "going forward" can be deleted.

A9) The expression "going forward" had been deleted.

E10) line 928: What is CFAD (perhaps I missed the definition?).

A10) The authors omitted to include a definition. The text now reads: "reflectivity contoured frequency by altitude diagrams (CFADs)"

(GO)²-SIM: A GCM-Oriented Ground-Observation Forward-Simulator Framework for Objective Evaluation of Cloud and Precipitation Phase

Katia Lamer¹, Ann M. Fridlind², Andrew S. Ackerman², Pavlos Kollias^{3,4,5}, Eugene E. Clothiaux¹ and Maxwell Kelley²

¹ Department of Meteorology and Atmospheric Science, Pennsylvania State University, University Park, 16802, U.S.A.

² NASA Goddard Institute for Space Studies, New York, 10025, U.S.A.

³ Environmental & Climate Sciences Department, Brookhaven National Laboratory, Upton, 11973, U.S.A.

⁴ School of Marine and Atmospheric Sciences, Stony Brook University, Stony Brook, 11794, U.S.A.

⁵ University of Cologne, Cologne, 50937, Germany

Correspondence to: Katia Lamer (kx15431@psu.edu)

Abstract

General circulation model (GCM) evaluation using ground-based observations is complicated by inconsistencies in hydrometeor and phase definitions. Here we describe (GO)²-SIM, a forward-simulator designed for objective hydrometeor phase evaluation, and assess its performance over the North Slope of Alaska using a one-year GCM simulation. For [uncertainty assessment](#), 18 empirical relationships are used to convert model grid-average hydrometeor (liquid and ice, cloud and precipitation) water contents to zenith polarimetric micropulse lidar and Ka-band Doppler radar measurements producing an ensemble of 576 forward-simulation realizations. Sensor limitations are represented in forward space to objectively remove from consideration model grid cells with undetectable hydrometeor mixing ratios, some of which may correspond to numerical noise.

Phase classification in forward space is complicated by the inability of sensors to measure ice and liquid signals distinctly. However, signatures exist in lidar-radar space such that thresholds on observables can be objectively estimated and related to hydrometeor phase. The proposed phase classification technique leads to misclassification in fewer than 8% of hydrometeor-containing grid cells. Such misclassifications arise because, while the radar is capable of detecting mixed-phase conditions, it can mistake water- for ice-dominated layers. However, applying the same classification algorithm to forward-simulated and observed fields should generate hydrometeor phase statistics with similar uncertainty. Alternatively, choosing to disregard how sensors define hydrometeor phase leads to frequency of occurrence discrepancies of up to 40%. So, while hydrometeor phase maps determined in forward space are very different from model “reality” they capture the information sensors can provide and thereby enable objective model evaluation.

Deleted: uncertainty quantification

50 **1 Introduction**

51

52

53

54

55

56

57

58

59

60

61

62

63

64

65

66

67

68

69

70

71

72

73

74

75

76

77

78

79

80

81

82

83

84

85

86

87

88

89

90

91

92

93

94

95

96

97

98

99

The effect of supercooled water on the Earth's top-of-atmosphere energy budget is a subject of increasing interest owing to its wide variability across climate models and its potential impact on predicted equilibrium climate sensitivity (Tan et al., 2016; McCoy et al., 2016; Frey et al., 2017). Some general circulation models (GCMs) now prognose number concentrations and mass mixing ratios for both cloud and precipitation hydrometeors of both liquid and ice phase, which enables them to shift towards more realistic microphysical process-based phase prediction (e.g., Gettelman and Morrison, 2015; Gettelman et al., 2015). While more complete and physically sound, these models still contain multiple scheme choices and tuning parameters, creating a need for increasingly thorough evaluation and adjustment (e.g., Tan and Storelvmo, 2016; English et al., 2014).

Active remote sensing observations remain an indirect approach to evaluate models because they measure hydrometeor properties different from those produced by microphysical schemes. For each hydrometeor species within a grid cell models prognose geophysical quantities such as mass and number concentration, whereas active remote sensors measure power backscattered from all hydrometeors species present within their observation volumes. Defining which hydrometeors have an impact is a fundamental question that needs to be addressed by the modeling, as well as observational, communities. In numerical models it is not uncommon to find very small hydrometeor mixing ratio amounts as demonstrated below. They may possibly be unphysical, effectively numerical noise, and the decision of which hydrometeor amounts are physically meaningful is somewhat arbitrary. Considering sensor capabilities is one path to objectively assessing hydrometeor populations within models. On such a path it is possible to evaluate those simulated hydrometeor populations that lead to signals detectable by sensors, leaving unassessed those not detected. Sensor detection capabilities are both platform- and sensor-specific. Space-borne lidars can adequately detect liquid clouds globally but their signals cannot penetrate thick liquid layers, limiting their use to a subset of single-layer systems or upper-level cloud decks (Hogan et al., 2004). Space-borne radar observations, while able to penetrate multi-layer cloud systems, are of coarser vertical resolution and of limited value near the surface owing to ground interference and low sensitivity (e.g., Huang et al., 2012b; Battaglia and Delanoë, 2013; Huang et al., 2012a). A perspective from the surface can therefore be more appropriate for the study of low-level cloud systems (e.g., de Boer et al., 2009; Dong and Mace, 2003; Klein et al., 2009; Intrieri et al., 2002).

Fortunately, both sensor sampling and hydrometeor scattering properties can be emulated through the use of forward-simulators. Forward-simulators convert model output to quantities observed by sensors and enable a fairer comparison between model output and observations; discrepancies can then be more readily attributed to dynamical and microphysical differences rather than methodological bias. For example, the CFMIP (Cloud Feedback Model Intercomparison Project) Observation Simulator Package (COSP) is composed of a number of satellite-oriented forward-simulators (Bodas-Salcedo et al., 2011), including a lidar backscattering forward-simulator that has been used to evaluate the representation of upper-level supercooled water layers in GCMs (e.g., Chepfer et al., 2008; Kay et al., 2016). Also, Zhang et al. (2017) present a first attempt at a ground-based radar reflectivity simulator tailored for GCM evaluation.

Here we propose to exploit the complementarity of ground-based vertically pointing polarimetric lidar and Doppler radar measurements, which have been shown uniquely capable of documenting water phase in shallow and multi-layered cloud conditions near the surface where supercooled water layers frequently form. More specifically, we present a GCM-oriented ground-based observation forward-simulator [(GO)²-SIM] framework designed for objective hydrometeor phase evaluation (Fig. 1). GCM output variables (Sec. 2) are converted to observables in three steps: 1) hydrometeor backscattered power estimation (Sec. 3), 2) consideration for sensor capabilities (Sec. 4) and, 3) estimation of specialized observables (Sec. 5). These forward-simulated fields, similar to observed fields, are used as inputs to a multi-sensor water phase

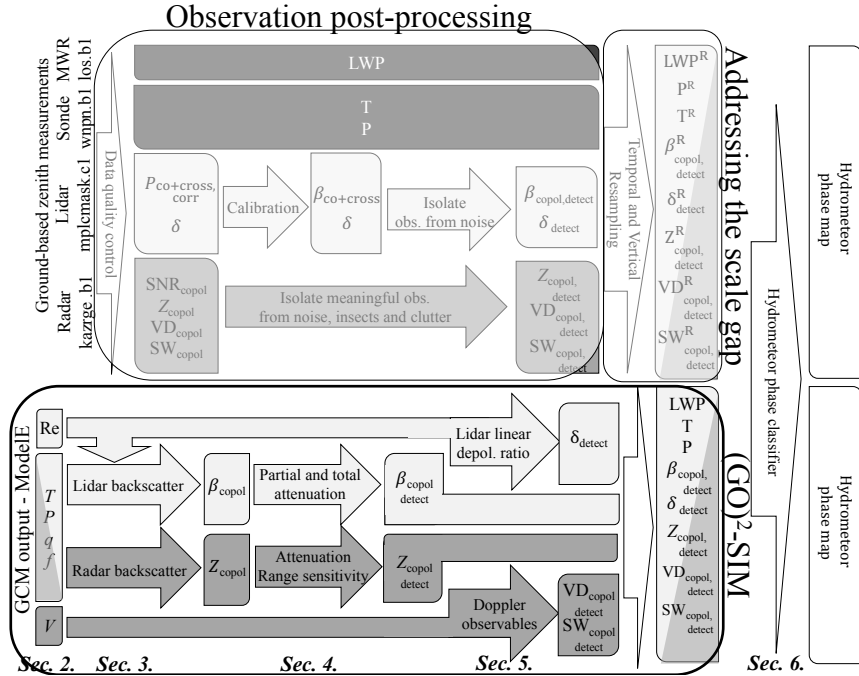
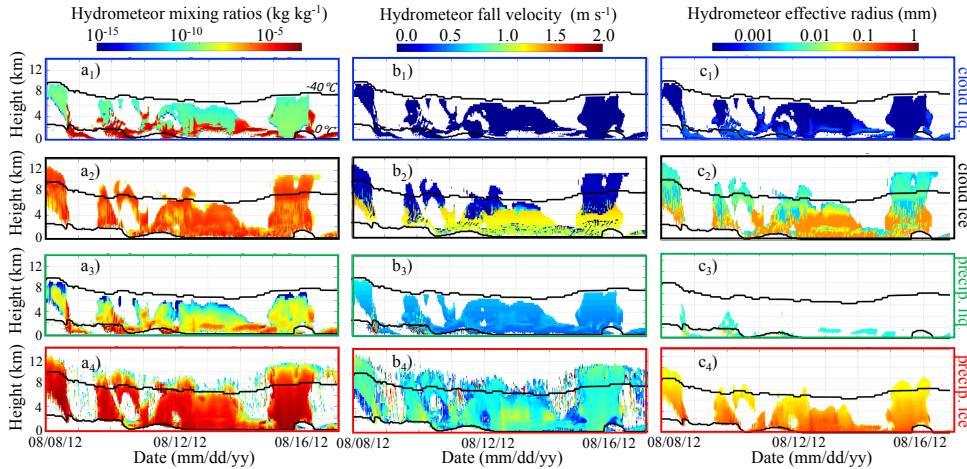


Figure 1. (GO)²-SIM framework. (GO)²-SIM emulates two types of remote sensors: Ka-band Doppler radars (dark gray shading) and 532 nm polarimetric lidars (light gray shading). It then tunes and applies a common phase-classification algorithm (white boxes) to both observed (upper section) and forward-simulated (bottom section) fields. Follow-on work will describe how observation can be post-processed and resampled to reduce the scale gap before model evaluation can be performed.

classifier (Sec. 6). The performance of (GO)²-SIM is evaluated over the North Slope of Alaska using output from a one-year simulation of the current development version of the NASA Goddard Institute for Space Studies GCM, hereafter referred to by its generic name, ModelE. Limitations and uncertainty are discussed in Sec. 6.3 and Sec. 7 respectively.

2 GCM Outputs Required as Inputs to the Forward-Simulator

To demonstrate how atmospheric model variables are converted to observables we performed a one-year global simulation using the current development version of the ModelE GCM. Outputs from a column over the North Slope of Alaska (column centered at latitude 71.00° and longitude -156.25°) are input to (GO)²-SIM. The most relevant changes from a recent version of ModelE (Schmidt et al. 2014) are implementation of the Bretherton and Park (2009) moist turbulence scheme and the Gettelman and Morrison (2015) microphysics scheme for stratiform cloud. The implementation of a two-moment microphysics scheme with prognostic precipitation species makes this ModelE version more suitable for the forward simulations presented here than previous versions. Here ModelE is configured with a 2.0° by 2.5° latitude-longitude grid with 62 vertical layers. The vertical grid varies with height from 10 hPa layer thickness over the bottom 100 hPa of the atmosphere, coarsening to about 50 hPa thickness in the mid-



126
127 **Figure 2.** Sample time series of ModelE outputs: a_{1-4} mixing ratios, b_{1-4} mass weighted fall speed
128 (positive values indicate downward motion) and c_{1-4} effective radii for cloud droplets (1; blue boxes),
129 cloud ice particles (2; black boxes), precipitating liquid drops (3; green boxes) and precipitating ice
130 particles (4; red boxes). Also indicated are the locations of the 0 °C and -40 °C isotherms (horizontal
131 black lines).

132
133
134 troposphere, and refining again to about 10 hPa thickness near the tropopause. For the current study, model
135 top is at 0.1 hPa, though we limit our analysis to pressures greater than 150 hPa. Dynamics (large scale
136 advection) is computed on a 225-s time step and column physics on a 30-min time step. High time-
137 resolution outputs (every column physics time step) are used as input to (GO)²-SIM. ModelE relies on two
138 separate schemes to prognose the occurrence of stratiform and convective clouds. The current study focuses
139 on stratiform clouds because their properties are more thoroughly diagnosed in this model version; when
140 performing future model evaluation, the contribution from convective clouds will also be considered.

141
142 An example of eight days of this simulation is displayed in Fig. 2. From a purely numerical modelling
143 standpoint, the simplest approach to defining hydrometeors is to consider any nonzero hydrometeor mixing
144 ratio as physically meaningful. Using this approach, we find that 43.5 % of the 981,120 grid cells simulated
145 in the one-year ModelE run contain hydrometeors, with 2.4 % of them being pure liquid, 37.8 % pure ice
146 and 59.8 % mixed in phase (Table 1a). However, these statistics are impacted by a number of simulated
147 small hydrometeor mixing ratio amounts that may or may not result from numerical noise (e.g., Fig. 2a;
148 blue-green colors). The forward-simulator framework will be used to create phase statistics of only those
149 hydrometeors present in amounts that can create signal detectable by sensors hence removing the need for
150 arbitrary filtering.

151
152 (GO)²-SIM forward-simulator inputs are, at model native resolution, mean grid box temperature and
153 pressure as well as hydrometeor mixing ratios, area fractions (used to estimate in-cloud values), mass
154 weighted fall speeds and effective radii for four hydrometeor species: cloud liquid water, cloud ice,
155 precipitating liquid water and precipitating ice. In its current setup, (GO)²-SIM can accommodate any
156 model that produces these output variables
157

159 3 Hydrometeor Backscattered Power Simulator

160

161 Reaching a common objective hydrometeor definition between numerical model output and active sensors
162 starts by addressing the fact that they are based on different hydrometeor properties (i.e., moments).
163 Backscattering amounts, observed by sensors, depend on both sensor frequency and on hydrometeors
164 properties and amounts. Hydrometeor properties that impact backscattering include size, phase,
165 composition, geometrical shape, orientation and bulk density. Were plausible representations for these
166 hydrometeor properties available as part of the model formulation, fundamental radiative transfer
167 calculations would be the most accurate way to transform model hydrometeor properties to observables.
168 However, in most GCMs such detailed hydrometeor information is highly simplified (e.g., fixed particle
169 size distribution shapes) or not explicitly represented (e.g., orientation and realistic geometrical shape),
170 complicating the process of performing direct radiative transfer calculations. Chepfer et al. (2008) proposed
171 an approach by which lidar backscattered power can be forward-simulated using model output hydrometeor
172 effective radius. Their approach, based on Mie theory, relies on the assumption that cloud particles (both
173 liquid and ice) are spherical and requires additional assumptions about hydrometeor size distributions and
174 scattering efficiencies. Similarly, the COSP (Bodas-Salcedo et al., 2011) and ARM Cloud Radar Simulator
175 for GCMs (Zhang et al., 2017) packages both use QuickBeam for the estimation of radar backscattered
176 power (i.e., radar reflectivity; Haynes et al., 2007). QuickBeam computes radar reflectivity using Mie
177 theory again under the assumption that all hydrometeor species are spherical and by making additional
178 assumptions about the shape of hydrometeor size distributions as well as mass-size and diameter-density
179 relationships. While some of these assumptions may be consistent with the assumptions in model cloud
180 microphysical parameterizations, some are not adequately realistic (e.g., spherical ice) or complete for
181 accurate backscattering estimation and it is typically very difficult to establish the sensitivity of results to
182 all such assumptions.

183

184 To avoid having to make ad hoc assumptions about hydrometeor shapes, orientations, and
185 compositions, which are properties that also remain poorly documented in nature, (GO)²-SIM employs
186 empirical relationships to convert model output to observables. These empirical relationships based on
187 observations, direct or retrieved with their own sets of underlying assumptions, are expected to capture at
188 least part of the natural variability in hydrometeor properties. Additionally empirical relationships are
189 computationally less expensive to implement than direct radiative scattering calculations, thus enabling the
190 estimation of an ensemble of backscattering calculations using a range of assumptions in an effort to
191 quantify part of the backscattering uncertainty (see Sec. 7). The empirical relationships proposed require
192 few model inputs, potentially enhancing consistency in applying (GO)²-SIM to models with differing
193 microphysics scheme assumptions and complexity. Section 6 will show that, while the empirical
194 relationships employed in (GO)²-SIM may not be as exact as direct radiative scattering calculations, they
195 produce backscattering estimates of sufficient accuracy for hydrometeor phase classification, which is the
196 main purpose of (GO)²-SIM at this time.

197

198 3.1 Lidar Backscattered Power Simulator

199

200 At a lidar wavelength of 532 nm, backscattered power is proportional to total particle cross section per
201 unit volume. Owing to their high number concentrations, despite their small size, cloud particles
202 backscatter [radiation of this wavelength](#) the most.

203

204 We adopt the Hu et al. (2007b) representation of liquid cloud extinction derived from CALIPSO and
205 CERES-MODIS observations and retrievals of liquid water content and effective radius (Table 2, Eq. 1).
206 For cloud ice water content, a number of empirical relationships with lidar extinction have been proposed
207 for various geophysical locations and ice cloud types using a variety of assumptions. Four of these
208 empirical relationships are implemented in (GO)²-SIM (Table 2, Eqns. 2-5 and references therein) and used

Deleted: scattering

Deleted: scattering

Deleted: this type of radiation

212 **Table 1.** a) Hydrometeor phase frequency of occurrence obtained a) from ModelE mixing ratios outside of
 213 the forward-simulator framework, b) and c) from the forward simulation ensemble created using different
 214 backscattered power assumptions. The median and interquartile range (IQR) capture the statistical behavior
 215 of the ensemble. Results using thresholds b) objectively determined for each forward ensemble member, c)
 216 modified from those in Shupe (2007). Percentage values are relative either to the total number of simulated
 217 hydrometeor-containing grid cells (426,603) or those grid cells with detectable hydrometeor amounts
 218 (333,927). Note that the total number of simulated grid cells analyzed is 981,120.

| a) Determined using ModelE Output Hydrometeor Mixing Ratios | | | | | | | | |
|---|---|-------------------|---|-------------------|--------------------------------------|-------------------|---|-------------------|
| | Grid cells containing only liquid phase | | Grid cells containing mixed phase | | Grid cells containing only ice phase | | Simulated hydrometeor-containing grid cells | |
| Frequency of Occurrence (%) | 2.4 | | 59.8 | | 37.8 | | 43.5 | |
| b) Determined Using Flexible Objective Thresholds from Model Output Mixing-Ratios | | | | | | | | |
| | Grid cells classified as liquid phase | | Grid cells classified as mixed phase | | Grid cells classified as ice phase | | Grid cells containing detectable hydrometeors | |
| | Median | $\frac{1}{2}$ IQR | Median | $\frac{1}{2}$ IQR | Median | $\frac{1}{2}$ IQR | Median | $\frac{1}{2}$ IQR |
| Frequency of Occurrence (%) | 11.3 | ± 0.6 | 19.2 | ± 1.8 | 68.8 | ± 3.1 | 78.3 | ± 1.8 |
| False Positive (%) | 0.5 | ± 0.0 | 1.1 | ± 0.3 | 0.0 | ± 0.0 | 1.7 | ± 0.3 |
| False Negative (%) | 0.2 | ± 0.0 | Approximately equal to sum of questionable row: (~ 5.2 \pm 0.9) | | 1.5 | ± 0.2 | 1.7 | ± 0.3 |
| Questionable (%) | 1.4 | ± 0.0 | | | 3.8 | ± 0.9 | 5.2 | ± 0.9 |
| Total Error (%) | | | | | | | 6.9 | ± 1.1 |
| c) Determined Using Fixed Empirical Thresholds Modified from Shupe (2007) | | | | | | | | |
| | Grid cells classified as liquid phase | | Grid cells classified as mixed phase | | Grid cells classified as ice phase | | Grid cells containing detectable hydrometeors | |
| | Median | $\frac{1}{2}$ IQR | Median | $\frac{1}{2}$ IQR | Median | $\frac{1}{2}$ IQR | Median | $\frac{1}{2}$ IQR |
| Frequency of Occurrence (%) | 12.5 | ± 0.4 | 13.1 | ± 2.4 | 71.5 | ± 3.7 | 78.2 | ± 1.8 |
| False Positive (%) | 0.5 | ± 0.0 | 0.3 | ± 0.0 | 0.1 | ± 0.0 | 0.9 | ± 0.0 |
| False Negative (%) | 0.1 | ± 0.0 | Approximately equal to sum of questionable row: (~ 6.7 \pm 1.1) | | 0.7 | ± 0.0 | 0.9 | ± 0.0 |
| Questionable (%) | 1.4 | ± 0.0 | | | 5.3 | ± 1.1 | 6.7 | ± 1.1 |
| Total Error (%) | | | | | | | 7.6 | ± 1.1 |

Deleted: ¶

Formatted Table

Deleted: ¶

Deleted: See questionable row

Formatted Table

Deleted: ¶

Deleted: See questionable row

220 to generate an ensemble of forward-simulations. Using these empirical relationships, a given water content
 221 can be mapped to a range of lidar extinction values (Fig. 3a). This spread depends both on the choice of
 222 empirical relationships and on the variability of the atmospheric conditions that affect them (i.e.,
 223 atmospheric temperature and hydrometeor effective radius variability). Fig. 3a also illustrates the
 224 fundamental idea that lidar extinction increases with increasing water content and that for a given water
 225 content cloud droplets generally lead to higher lidar extinction than cloud ice particles.
 226

227 Lidar co-polar backscattered power ($\beta_{\text{copol,species}}$ [$\text{m}^{-1}\text{sr}^{-1}$]) generated by each hydrometeor species is
 228 related to lidar extinction ($\sigma_{\text{copol,species}}$ [m^{-1}]) through the lidar ratio (S_{species} [sr]):
 229

230
$$\beta_{\text{copol,cl}} = (1/S_{\text{cl}}) \sigma_{\text{copol,cl}} \tag{6}$$

231
$$\beta_{\text{copol,ci}} = (1/S_{\text{ci}}) \sigma_{\text{copol,ci}} \tag{7}$$

238 While constant values are used for the lidar ratios of liquid and ice clouds in this version of the forward-
 239 simulator, we acknowledge that in reality they depend on particle size. O'Connor et al. (2004) suggest that a
 240 liquid cloud lidar ratio (S_{cl}) of 18.6 sr is valid for cloud liquid droplets smaller than 25 μm , which
 241 encompasses the median diameter expected in the stratiform clouds simulated here. Kuehn et al. (2016)
 242 observed layer-averaged lidar ratios in ice clouds (S_{ci}) ranging from 15.1 to 36.3 sr. Sensitivity tests
 243 indicate that adjusting the ice cloud lidar ratio to either of these extreme values in the forward-simulator
 244 increases the number of detectable hydrometeors by no more than 0.6 %, changes the hydrometeor phase
 245 frequency of occurrence statistics by less than 0.4% and causes less than a 0.1% change in phase-
 246 classification errors (not shown). Given these results, the ice cloud lidar ratio is set to the constant value of
 247 25.7 sr, which corresponds to the mean value observed by Kuehn et al. (2016).
 248

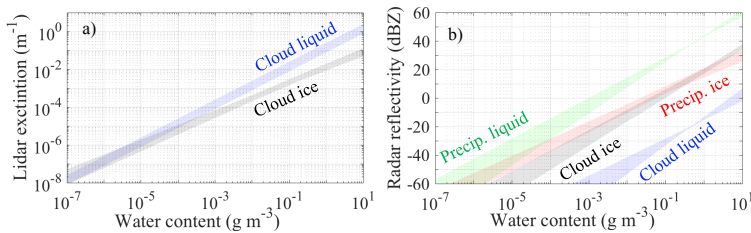
249 It is important to consider that lidars do not measure cloud droplet backscattering independently of cloud
 250 ice particle backscattering. Rather they measure total co-polar backscattered power ($\beta_{\text{copol,total}}$) which is
 251 the sum of the contribution from both cloud phases.
 252

253 3.2 Radar Backscattered Power Simulator

254
 255 At the cloud-radar wavelength of 8.56 mm (Ka-band), backscattered power is approximately related to
 256 the sixth power of the particle diameter, and inversely proportional to the forth power of the wavelength.
 257 Hereafter radar backscattered power will be referred to as “radar reflectivity” as commonly done in
 258 literature.
 259

260 (GO)²-SIM relies on water content-based empirical relationships to estimate cloud liquid water (cl), cloud
 261 ice (ci), precipitating liquid water (pl) and precipitating ice (pi) radar reflectivity. Different relationships are
 262 used for each species to account for the fact that hydrometeor mass and size both affect radar reflectivity. A
 263 number of empirical relationships link hydrometeor water content to co-polar radar reflectivity. Thirteen of
 264 these empirical relationships are implemented in (GO)²-SIM (Table 2, Eqns. 8-20 and references therein)
 265 and used to generate an ensemble of forward-simulations. Figure 3b illustrates the fact that for all these
 266 empirical relationships increasing water content leads to increasing radar reflectivity. As already
 267 mentioned, radar reflectivity is approximately related to the sixth power of the particle size, which explains
 268 why, for the same water content, precipitating hydrometeors are associated with greater reflectivity than
 269 cloud hydrometeors.
 270

271 In reality, radars cannot isolate energy backscattered by individual hydrometeor species. Rather they
 272 measure total co-polar reflectivity ($Z_{\text{copol,total}}$ [$\text{mm}^6 \text{m}^{-3}$]) which is the sum of the contributions from all
 273 of the hydrometeor species.



274
 275 **Figure 3.** Relationship between water content in the form of cloud liquid (blue), precipitating liquid
 276 (green), cloud ice (black) and precipitating ice (red) and a) Lidar extinction, and b) Radar co-polar
 277 reflectivity. Spread emerges from using multiple differing empirical relationships (listed in Table 2) and
 278 from variability in the one-year ModelE output (including the effects of varying temperature and effective
 279 radii).

280 **Table 2.** Empirical relationships used to convert hydrometeor water content (WC [g m⁻²]) to lidar
 281 extinction (σ [m⁻¹]) and radar reflectivity (Z [mm⁶ m⁻³]).
 282

| Type | Eq. # | Relationships for lidar extinction | References |
|----------------------|-------|--|------------------------------|
| Cloud liq. (cl) | 1 | $\sigma_{\text{copol,cl}} = \frac{\text{WC}_{\text{cl}}(3/2)}{\text{Re } \rho_{\text{liq}}}$ with $\rho_{\text{liq}} = 1$ | Hu et al. (2007b) |
| | 2 | $\sigma_{\text{copol,cl}} = \left(\frac{\text{WC}_{\text{cl}}}{119}\right)^{1/1.22}$ | Heymsfield et al. (2005) |
| Cloud ice (ci) | 3 | $\sigma_{\text{copol,ci}} = \left(\frac{\text{WC}_{\text{ci}}}{a_3}\right)^{1/b_3}$ with $a_3 = 89 + 0.6204T$ and $b_3 = 1.02 - 0.0281T$ | Heymsfield et al. (2005) |
| | 4 | $\sigma_{\text{copol,ci}} = \left(\frac{\text{WC}_{\text{ci}}}{527}\right)^{1/1.32}$ | Heymsfield et al. (2014) |
| | 5 | $\sigma_{\text{copol,ci}} = \left(\frac{\text{WC}_{\text{ci}}}{a_2}\right)^{1/b_2}$ with $a_2 = 0.00532 * (T + 90)^{2.55}$ and $b_2 = 1.31e^{(0.0047T)}$ | Heymsfield et al. (2014) |
| Type | Eq. # | Relationships for radar reflectivity | References |
| Cloud liq. (cl) | 8 | $Z_{\text{copol,cl}} = 0.048 \text{WC}_{\text{cl}}^{2.00}$ | Atlas (1954) |
| | 9 | $Z_{\text{copol,cl}} = 0.03 \text{WC}_{\text{cl}}^{1.31}$ | Sauvageot and Omar (1987) |
| | 10 | $Z_{\text{copol,cl}} = 0.031 \text{WC}_{\text{cl}}^{1.56}$ | Fox and Illingworth (1997) |
| Cloud ice (ci) | 11a | $Z_{\text{copol,ci}} = 10^{\left(\frac{\log_{10}(\text{WC}_{\text{ci}})+1.70+0.0233T}{0.072}\right)/10}$ | R. J. Hogan et al. (2006) |
| | 12 | $Z_{\text{copol,ci}} = \left(\frac{\text{WC}_{\text{ci}}}{0.064}\right)^{\frac{1}{0.58}}$ | Atlas et al. (1995) |
| | 13 | $Z_{\text{copol,ci}} = \left(\frac{\text{WC}_{\text{ci}}}{0.097}\right)^{\frac{1}{0.59}}$ | Liu and Illingworth (2000) |
| | 14 | $Z_{\text{copol,ci}} = \left(\frac{\text{WC}_{\text{ci}}}{0.037}\right)^{\frac{1}{0.696}}$ | Sassen (1987) |
| Precip. liq. (pl) | 15 | $Z_{\text{copol,pl}}[\text{mm}^6 \text{m}^{-3}] = \left(\frac{\text{WC}_{\text{pl}}}{0.0034}\right)^{\frac{7}{4}}$ | Hagen and Yuter (2003) |
| | 16 | $Z_{\text{copol,pl}}[\text{mm}^6 \text{m}^{-3}] = \left(\frac{\text{WC}_{\text{pl}}}{0.0039}\right)^{\frac{1}{0.55}}$ | Battan (1973) |
| | 17 | $Z_{\text{copol,pl}} = \left(\frac{\text{WC}_{\text{pl}}}{0.00098}\right)^{\frac{1}{0.7}}$ | Sekhon and Srivastava (1971) |
| Precip. ice (pi) | 11b | $Z_{\text{copol,pi}} = 10^{\left(\frac{\log_{10}(\text{WC}_{\text{pi}})+1.70+0.0233T}{0.072}\right)/10}$ | R. J. Hogan et al. (2006) |
| | 18 | $Z_{\text{copol,pi}} = \left(\frac{\text{WC}_{\text{pi}}}{0.0218}\right)^{\frac{1}{0.79}}$ | Liao and Sassen (1994) |
| | 19 | $Z_{\text{copol,pi}} = \left(\frac{\text{WC}_{\text{pi}}}{0.04915}\right)^{\frac{1}{0.90}}$ | Sato et al. (1981) |
| | 20 | $Z_{\text{copol,pi}} = \left(\frac{\text{WC}_{\text{pi}}}{0.05751}\right)^{\frac{1}{0.736}}$ | Kikuchi et al. (1982) |

283 4 Sensor Capability Simulator

284

285 In the previous section, total backscattered power resulting from all modeled hydrometeor species
286 (without any filtering) is estimated. In order to objectively assess model hydrometeor properties, they must
287 be converted to quantities that are comparable to observations, necessitating incorporation of sensor
288 detection limitations, including attenuation and finite sensitivity. Fortunately, lidar and radar sensors are
289 often relatively well-characterized so that sensor detection capabilities can be quantified and replicated in
290 forward-simulators for an objective model-to-observation comparison.

291

292 4.1 Lidar Detection Capability

293

294 Following the work of Chepfer et al. (2008), the (GO)²-SIM lidar forward-simulator takes into
295 consideration that lidar power is attenuated by clouds. Attenuation is related to cloud optical depth (τ),
296 which is a function of total cloud extinction ($\sigma_{\text{copol,total}}$ [m^{-1}]) that includes the effect of cloud liquid
297 water and cloud ice via:

298

$$299 \tau = \int_{z_0}^z \sigma_{\text{copol,total}} dh, \quad (21)$$

300

301 Lidar attenuation is exponential and two-way as it affects the lidar power on its way out and back:

302

$$303 \beta_{\text{copol,total,att}} = \beta_{\text{copol,total}} e^{-2\eta\tau}. \quad (22)$$

304

305 Note that in some instances multiple scattering occurs before the lidar signal returns to the sensor, thus
306 amplifying the returned signal. In theory, the multiple scattering coefficient (η) varies from 0 to 1. Sensors
307 with large fields of view, such as satellite-based lidars, are more likely to be impacted by multiple
308 scattering than others (Winker, 2003). In the current study, for which a ground-based lidar is simulated, a
309 multiple scattering coefficient of unity is used. A sensitivity test in which this coefficient was varied from
310 0.7, such as that implemented in the CALIPSO satellite lidar simulator of Chepfer et al. (2008), to 0.3,
311 representing an extreme case, indicated that multiple scattering had a negligible impact (less than 1%) on
312 the number of hydrometeors detected, the hydrometeor phase frequency of occurrence statistics, and in
313 phase classification error (not shown).

314

315 In the current simulator we assume that only cloud segments with optical depth smaller than three can be
316 penetrated, other clouds being opaque (Cesana and Chepfer, 2013) such that total co-polar backscattered
317 power detected ($\beta_{\text{copol,total,detect}}$) is:

318

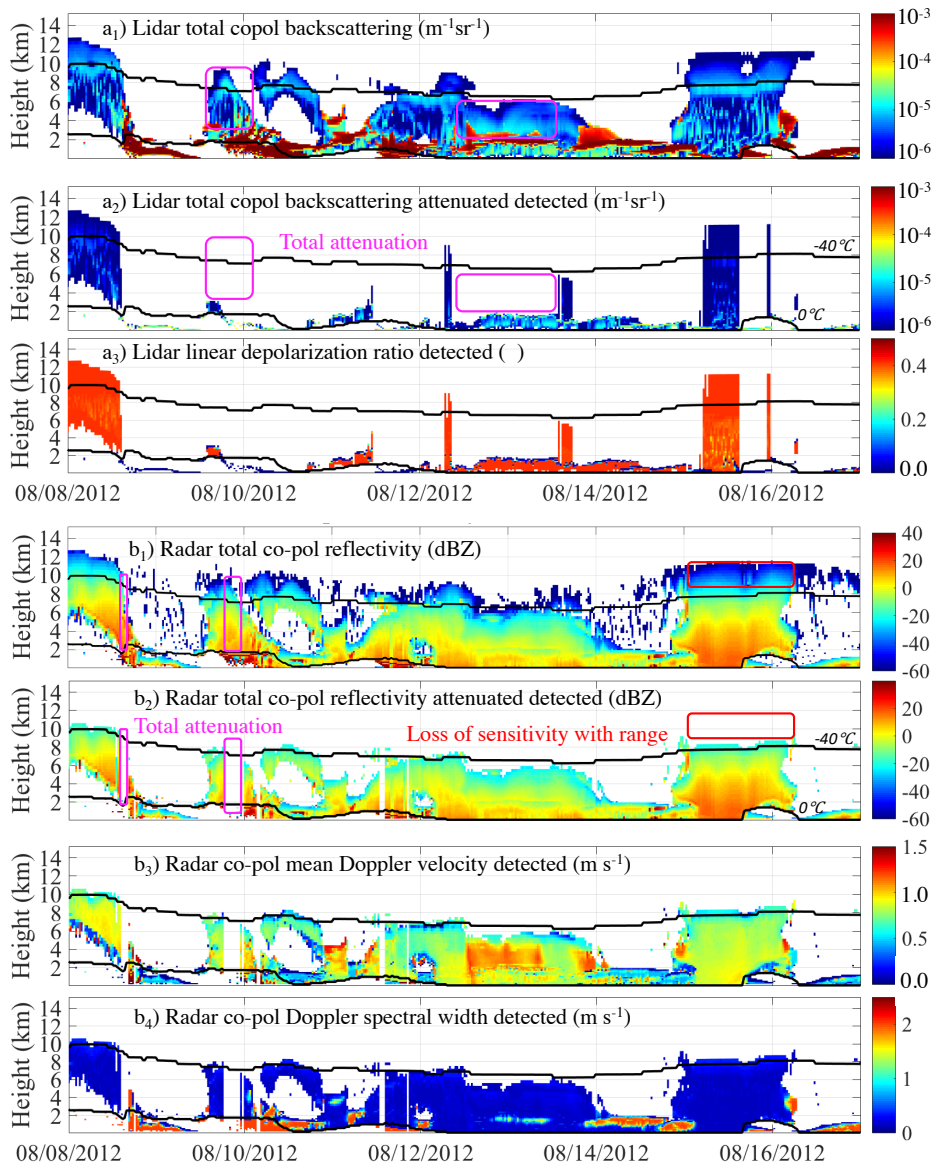
$$319 \beta_{\text{copol,total,detect}} = \beta_{\text{copol,total,att}} \quad \text{where } \tau \leq 3; \\ 320 \beta_{\text{copol,total,detect}} = \text{undetected} \quad \text{where } \tau > 3. \quad (23)$$

321

322 For the sample ModelE output shown in Fig. 2, Fig. 4a illustrates results from the lidar forward-simulator
323 for one forward-ensemble member (i.e., using a single set of lidar backscattered power empirical
324 relationships specifically eqns. (1) and (4)). Figure 4a₁ shows lidar total co-polar backscattered power
325 without consideration of sensor limitations, such as attenuation, which are included in Fig. 4a₂. Lidar
326 attenuation prevents the tops of deep systems containing supercooled water layers from being observed
327 (e.g., magenta boxes on 08/10 and 08/13). For the one-year sample the forward-simulated lidar system
328 detects only 35.5% of simulated hydrometeor-containing grid cells. In Sec. 6 we will determine which
329 hydrometeors (liquid water or ice) are responsible for the detected signals.

330

331



332
 333 **Figure 4.** Example outputs from the (GO)²-SIM backscattered power modules (1), sensor capability
 334 modules (2) and specialized-observables modules (3-4) for a) lidars and b) radars obtained using one set of
 335 empirical backscattered power relationships. This figure highlights sensor limitations ranging from
 336 attenuation (magenta boxes) to sensitivity loss with range (red boxes). Also indicated are the locations of
 337 the 0 °C and -40 °C isotherms (black lines). Note that positive velocities indicate downward motion.

338 4.2 Radar Detection Capability

339

340 Millimeter-wavelength radars are also affected by signal attenuation. Radar signal attenuation depends
341 both on the transmitted wavelength and on the mass and phase of the hydrometeors. Liquid phase
342 hydrometeors attenuate radar signals at all millimeter radar wavelengths, even leading to total signal loss in
343 heavy rain conditions. In contrast, water vapor attenuation is less important at relatively longer wavelengths
344 (e.g., 8.56 mm; the wavelength simulated here) but can be important near wavelengths of 3.19 mm (the
345 CloudSat operating wavelength; (Bodas-Salcedo et al., 2011)).

346

347 At 8.56 mm (Ka-band) total co-polar attenuated reflectivity ($Z_{\text{copol,total,att}}$ [dBZ]) is given by:

348

$$349 Z_{\text{copol,total,att}} = Z_{\text{copol,total}} - 2 \int_{z=0}^z [a (WC_{\text{pl}} + WC_{\text{cl}})] dh, \quad (24)$$

350

351 where attenuation is controlled by the wavelength-dependent attenuation coefficient a ($[\text{dB km}^{-1} (\text{g m}^{-3})^{-1}]$)
352 which we take to be 0.6 at Ka-band (Ellis and Vivekanandan, 2011), by the water contents of cloud liquid
353 ($WC_{\text{cl}} [\text{g m}^{-3}]$) and precipitating liquid ($WC_{\text{pl}} [\text{g m}^{-3}]$), and by the thickness of the liquid layer.

354

355 In addition to attenuation, radars suffer from having a finite sensitivity that decreases with distance. Given
356 this, the total co-polar reflectivity detectable ($Z_{\text{copol,total,detect}}$ [dBZ]) is

357

$$358 Z_{\text{copol,total,detect}} = Z_{\text{copol,total,att}} \text{ where } Z_{\text{copol,total,att}} \geq Z_{\text{min}}, \\ 359 Z_{\text{copol,total,detect}} = \text{Undetected} \text{ where } Z_{\text{copol,total,att}} < Z_{\text{min}}, \quad (25a)$$

360

361 where the radar minimum detectable signal (Z_{min} [dBZ]) is a function of height (h [km]) and can be
362 expressed as

363

$$364 Z_{\text{min}} = Z_{\text{sensitivity at 1 km}} + 20 \log_{10} h. \quad (25b)$$

365

366 A value of $Z_{\text{sensitivity at 1 km}} = -41$ dBZ is selected to reflect the sensitivity of the Ka-band ARM Zenith
367 Radar (KAZR) currently installed at the Atmospheric Radiation Measurement (ARM) North Slope of
368 Alaska observatory. This value has been determined by monitoring two years of observations and it reflects
369 the minimum signal observed at a height of 1 km. The minimum detectable signal used in the simulator
370 should reflect the sensitivity of the sensor used to produce the observational benchmark to be compared to
371 the forward-simulator output.

372

373 For the sample ModelE output shown in Fig. 2, Figure 4b illustrates results from the radar forward-
374 simulator for one forward-ensemble member (i.e., using a single set of radar reflectivity empirical
375 relationships specifically eqns. (9), (11a), (15) and (11b)). Figure 4b₁ shows radar total co-polar reflectivity
376 without consideration of sensor limitations, while Fig. 4b₂ includes the effects of attenuation and the range-
377 dependent minimum detectable signal. Sensor limitations make it such that heavy rain producing systems
378 cannot be penetrated (e.g., magenta box on 08/08 and 08/10) and the tops of deep systems cannot be
379 observed (e.g., red box on 08/15). For the one-year sample the forward-simulated radar system could detect
380 only 69.9 % of the simulated hydrometeor-containing grid cells. In Sec. 6 we will determine the phase of
381 the hydrometeors responsible for the detected signals.

382

383 4.3 Lidar-Radar Complementarity

384

385 Figures 4a₂ and 4b₂ highlight the complementarity of lidar and radar sensors. Despite sensor
386 limitations, 532 nm lidar measurements can be used to characterize hydrometeors near the surface and infer

387 the location of a lowermost liquid layer if one exists. In contrast, 8.56 mm radars have the ability to
 388 penetrate cloud layers and light precipitation, allowing them to determine cloud boundary locations (e.g.,
 389 Kollias et al., 2016). For the one-year sample ModelE output the combination of both sensors enables
 390 detection of 73.0 % of the hydrometeor-containing grid cells. Real observations can be used to objectively
 391 evaluate these detectable hydrometeor populations while nothing can be said about those that are not
 392 detectable. Note that a number of undetectable grid cells only contain trace amounts of hydrometeors,
 393 which could be the result of numerical noise. As such the approach of considering sensor detection
 394 limitations helps objectively remove numerical noise from consideration and allows model and
 395 observations to converge towards a common hydrometeor definition for a fair comparison.

396 **5 Forward Simulation of Specialized Observables**

397 In the previous section total co-polar backscattered powers are used to determine which simulated
 398 hydrometeors are present in sufficient amounts to be detectable by sensors hence removing numerical noise
 399 from consideration. However, determining the phase of the detectable hydrometeor populations can be
 400 achieved with much greater accuracy by using additional observables.

401 Backscattered power alone provides a sense of hydrometeor number concentration (from lidar) and
 402 hydrometeor size (from radar), but it does not contain information about hydrometeor shape nor does it
 403 provide any hint on the number of coexisting hydrometeor species, both of which are relevant for phase
 404 determination. However, such information is available from lidar depolarization ratios and radar Doppler
 405 spectral widths.

406 **5.1 Lidar Depolarization Ratio Simulator**

407 So far we have described how hydrometeors of all types and phases affect co-polar radiation. It is
 408 important to note that radiation also has a cross-polar component which is only affected by nonspherical
 409 particles. Ice particles, which tend to be nonspherical, are expected to affect this component while we
 410 assume that cloud droplets, which tend to be spherical, do not. Taking the ratio of cross-polar to co-polar
 411 backscattering thus provides information about the dominance of ice particles in a hydrometeor population.
 412 This ratio is referred to as the linear depolarization ratio (δ_{detect}) and it can be estimated where
 413 hydrometeors are detected by the lidar.

$$414 \delta_{\text{detect}} = \frac{\beta_{\text{crosspol,ci,detect}} + \beta_{\text{crosspol,cl,detect}}}{\beta_{\text{copol,total,detect}}}. \quad (26a)$$

415 According to an analysis of CALIPSO observations by Cesana and Chepfer (2013), cloud ice particle
 416 cross-polar backscattering ($\beta_{\text{crosspol,ci,detect}}$ [$\text{m}^{-1}\text{sr}^{-1}$]) and cloud liquid droplet cross-polar
 417 backscattering ($\beta_{\text{crosspol,cl,detect}}$ [$\text{m}^{-1}\text{sr}^{-1}$]) can be approximated using the following relationships:

$$418 \beta_{\text{crosspol,ci,detect}} = 0.29 (\beta_{\text{copol,ci,detect}} + \beta_{\text{crosspol,ci,detect}}), \quad (26b)$$

$$419 \beta_{\text{crosspol,cl,detect}} = 1.39 (\beta_{\text{copol,cl,detect}} + \beta_{\text{crosspol,cl,detect}}) \\ 420 + 1.76 \cdot 10^{-2} (\beta_{\text{copol,cl,detect}} + \beta_{\text{crosspol,cl,detect}}) \approx 0. \quad (26c)$$

421 For reasons mentioned in Sec. 4.1, multiple scattering is considered negligible in the current study such that
 422 cloud-liquid droplet cross-polar backscattering is assumed to be zero under all conditions.

435 **5.2 Radar Doppler Moment Simulator**

436

437 Specialty Doppler radars have the capability to provide information about the movement of
 438 hydrometeors in the radar observation volume. This information comes in the form of the radar Doppler
 439 spectrum, which describes how backscattered power is distributed as a function of hydrometeor velocity
 440 (Kollias et al., 2011). The zeroth moment of the Doppler spectral distribution (the spectral integral) is radar
 441 reflectivity, the first moment (the spectral mean) is mean Doppler velocity (VD) and the second moment
 442 (the spectral spread) is Doppler spectral width (SW). Rich information is provided by the velocity spread
 443 (i.e., SW) of the hydrometeor population including information regarding the number of coexisting species,
 444 turbulence intensity and spread of the hydrometeor particle size distributions. Typically, the effects of
 445 turbulence and hydrometeor size variations on the velocity spread for a single species are much smaller
 446 than the effect of mixed-phase conditions. As such, Doppler spectral width is a useful parameter for
 447 hydrometeor phase identification.

448

449 Forward-simulations of Doppler quantities have been performed for cloud models using bin microphysics
 450 (e.g., Tatarevic and Kollias, 2015) but not, to our knowledge, for GCMs using 2-moment microphysics
 451 schemes. Co-polar mean Doppler velocity and co-polar Doppler spectral width are subject to the same
 452 detection limitations as radar reflectivity. In fact, just like radar reflectivity, these observables are strongly
 453 influenced by large hydrometeors; that is, they are reflectivity-weighted velocity averages.

454

455 Our approach begins by quantifying the contribution of each species present (P_{species}), which is determined
 456 by the species detected co-polar reflectivity ($Z_{\text{copol,species,detect}}$ [$\text{mm}^6 \text{m}^{-3}$]) relative to the total detected
 457 co-polar reflectivity ($Z_{\text{copol,total,detect}}$ [$\text{mm}^6 \text{m}^{-3}$]):

458

459
$$P_{\text{species}} = \frac{Z_{\text{copol,species,detect}}}{Z_{\text{copol,total,detect}}}, \quad (27a)$$

460

461 together with

462

463
$$Z_{\text{copol,species,detect}} = Z_{\text{copol,species}} - 2 \int_{z=0}^z [a (WC_{\text{pl}} + WC_{\text{ci}})] dh \quad \text{where } Z_{\text{copol,total,att}} \geq Z_{\text{min}}. \quad (27b)$$

464

465 In Eqns. 27a-b the subscript “species” represents cl, ci, pl, or pi. The attenuation coefficient (a), minimum
 466 detectable signal (Z_{min}) and water contents (WC) are as in Eq. 24. Total mean Doppler velocity detected
 467 ($VD_{\text{copol,detect}}$ [m s^{-1}]) is the reflectivity-weighted sum of the mass-weighted fall velocity of each
 468 hydrometeor species (V_{species} [m s^{-1}]):

469

470
$$VD_{\text{copol,detect}} = \sum_{\text{species=cl,pl,ci,pi}} P_{\text{species}} V_{\text{species}}, \quad (28)$$

471

472 where the mass-weighted fall velocity of each hydrometeor species (V_{species} [m s^{-1}]) is a model output.
 473 Total Doppler spectral width ($SW_{\text{copol,detect}}$ [m s^{-1}]) is more complex and can be estimated following a
 474 statistical method similar to that described by Everitt and Hand (1981). It takes into consideration the
 475 properties of each individual hydrometeor species through their respective fall speed (V_{species} [m s^{-1}]) and
 476 spectral width (SW_{species} [m s^{-1}]) in relation to the properties of the hydrometeor population as a whole
 477 through the total mean Doppler velocity detected ($VD_{\text{copol,detect}}$) estimated in Eq. 28:

478

479
$$SW_{\text{copol,detect}} = \sqrt{\sum_{\text{species=cl,pl,ci,pi}} P_{\text{species}} (SW_{\text{species}}^2 + (V_{\text{species}} - VD_{\text{copol,detect}})^2)}, \quad (29)$$

Deleted: $\sum_{\text{species=cl,pl,ci,pi}} P_{\text{species}} (SW_{\text{species}}^2 + (V_{\text{species}} - VD_{\text{copol,detect}})^2)$,

Deleted:

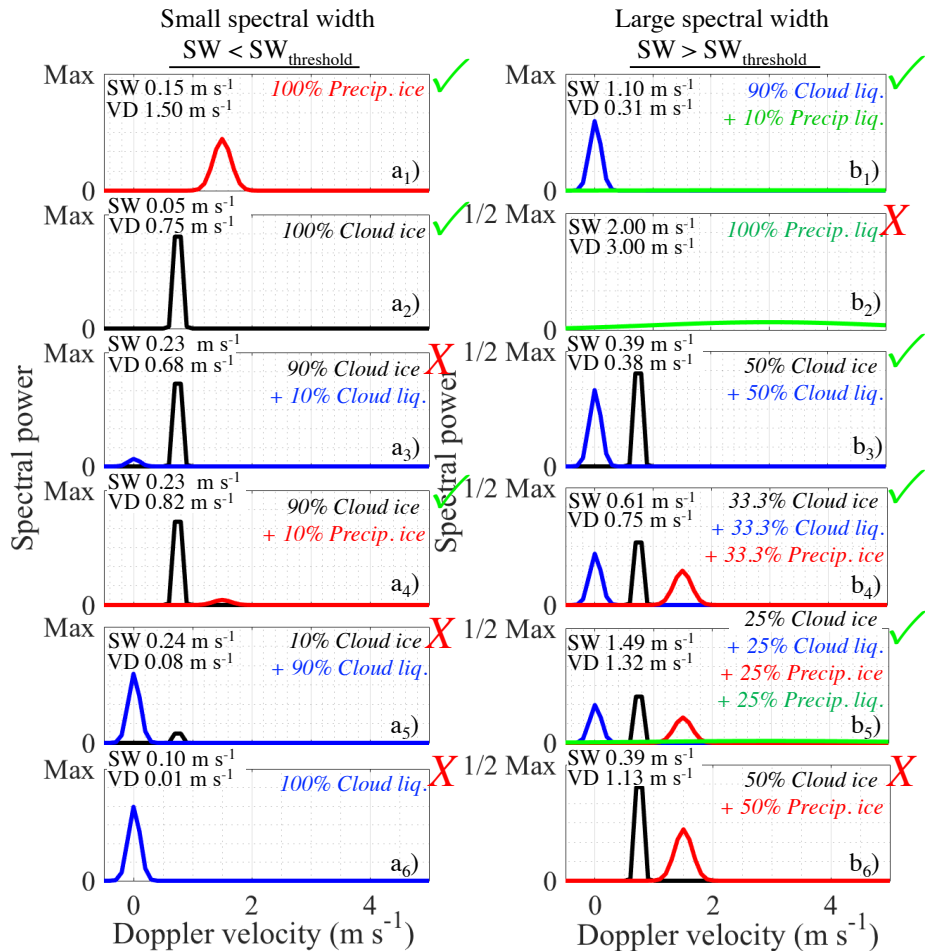
483 where the spectral widths of individual species (SW_{species}) are assigned climatological values. These
484 climatological values are $SW_{\text{cl}} = 0.10 \text{ m s}^{-1}$, $SW_{\text{ci}} = 0.05 \text{ m s}^{-1}$, $SW_{\text{pi}} = 0.15 \text{ m s}^{-1}$ and $SW_{\text{pl}} =$
485 2.00 m s^{-1} (Kalesse et al., 2016).
486

487 For the sample ModelE output shown in Fig. 2, Figs. 4b₃ and 4b₄ respectively show examples of forward
488 simulated mean Doppler velocity and Doppler spectral width estimate using one set of empirical radar
489 reflectivity relationship.
490

491 **6 Water Phase Classifier Algorithm**

492
493 From a purely numerical modeling perspective the simplest approach to defining the phase of a
494 hydrometeor population contained in grid cells is to consider that any nonzero hydrometeor mixing ratio
495 species contributes to the phase of the population. Using this approach, in the one-year sample, we find that
496 the detectable hydrometeor-containing grid cells are 2.4 % pure liquid, 19.4 % pure ice and 78.2 % mixed
497 phase (Note how these water phase statistics differ by up to 18.4 % from Sec. 2 where all grid cells,
498 potentially including numerical noise, were considered). But determining hydrometeor phase in
499 observational space is not as straightforward. It is complicated by the fact that sensors do not record ice-
500 and liquid-hydrometeor returns separately but rather record total backscattering from all hydrometeors.
501 Retrieval algorithms are typically applied to the observed total backscattering to determine the phase of
502 hydrometeor populations. However, phase classification algorithms have limitations that require each
503 hydrometeor species to be present not only in nonzero amounts but in amounts sufficient to produce a
504 phase signal. Thus, hydrometeor phase statistics obtained from a numerical model in the absence of a
505 forward simulator are not necessarily comparable with equivalent statistics retrieved from observables,
506 especially in instances where one hydrometeor species dominates the grid cell and other species are present
507 in trace amounts. A common hydrometeor phase definition must be established to objectively evaluate the
508 phase of simulated hydrometeor populations using observations, which requires the development of a phase
509 classification algorithm that can be applied to observables both forward-simulated and real.
510

511 The scientific literature contains a number of phase classification algorithms with different levels of
512 complexity. Hogan et al. (2003) used regions of high lidar backscattered power as an indicator for the
513 presence of liquid droplets. Lidar backscattered power combined with lidar linear depolarization ratio has
514 been used to avoid some of the misclassifications encountered when using backscattered power alone (e.g.,
515 Yoshida et al., 2010; Hu et al., 2007a; Hu et al., 2009; Hu et al., 2010; Sassen, 1991). Hogan and O'Connor
516 (2004) proposed using lidar backscattered power in combination with radar reflectivity. While the
517 combination of radar and lidar backscattered powers is useful for the identification of mixed-phase
518 conditions, their combined extent remains limited to single layer clouds or to lower cloud decks because of
519 lidar signal attenuation. Shupe (2007) proposed a technique in which radar Doppler velocity information is
520 used as an alternative to lidar backscattering information (for ranges beyond that of lidar total attenuation)
521 to infer the presence of supercooled water in multi-layer systems. Figure 5 displays cartoons of Doppler
522 spectra that have the same total co-polar radar reflectivity but different total mean Doppler velocities (VD)
523 and Doppler spectral widths (SW) resulting from different hydrometeor species and combinations, thus
524 highlighting the added value of Doppler information. The contribution of each species to the total co-polar
525 reflectivity is indicated as a percentage in the top right of each subpanel. These scenarios show that VD
526 tends to be relatively small for pure liquid cloud (Fig. 5a₆), pure ice cloud (Fig. 5a₂), and even mixed-phase
527 non-precipitating cloud (Fig. 5a₃,a₅,b₃) and only tends to increase when precipitation is present in cloud
528 (Fig. 5 a₄,b₃,b₄,b₅) or below cloud (Fig. 5a₁,b₂), making VD a seemingly robust indicator for precipitation
529 occurrence but not for phase identification. These scenarios also show that SW tends to be relatively small
530 in single-phase clouds without precipitation (Fig. 5a₂,a₆), pure precipitating ice (Fig. 5a₁) and multi-species
531 clouds with a dominant hydrometeor species (Fig. 5a₃,a₅). On the other hand, SW tends to be large when
532



533
534
535
536
537
538
539
540
541
542
543
544
545
546

Figure 5. Cartoon examples of radar Doppler spectra from different hydrometeors combinations: precipitating ice (red), cloud ice (black), precipitating water (green) and cloud water (blue). The contribution of each hydrometeor species to the total co-polar reflectivity is indicated in the top right of each subpanel. Each radar Doppler spectrum has been normalized to have the same total co-polar radar reflectivity which highlights that different hydrometeor combinations generate unique mean Doppler velocity (VD) and Doppler spectral width (SW) signatures. As discussed in Sec. 6, low spectral width signatures are assumed to be associated with ice conditions (column a) while high spectral width signatures are assumed to be associated with liquid/mixed-phase conditions (column b). Hydrometeor combinations that respect these assumptions are marked with ✓-marks. Exceptions to these rules (✗-marks) are responsible for (GO)²-SIM phase misclassifications above the level of lidar extinction. This list is not exhaustive.

547 liquid precipitation is present (Fig. 5b₁,b₂,b₅) and in mixed-phase clouds without a dominant species (Fig.
548 5b₃,b₄,b₅). These scenarios suggest that large spectral widths are useful indicators for the presence of
549 supercooled rain and mixed-phase conditions. Scenarios where this interpretation of spectrum width is
550 incorrect will be discussed in Sec. 6.3.

551
552 Regardless of which observation they are based-on, the aforementioned phase classification schemes all
553 rely on assumption that hydrometeor phases when projected on observational space (e.g., lidar
554 backscattered power against lidar depolarization ratio) create well-defined patterns that can be separated
555 using thresholds.

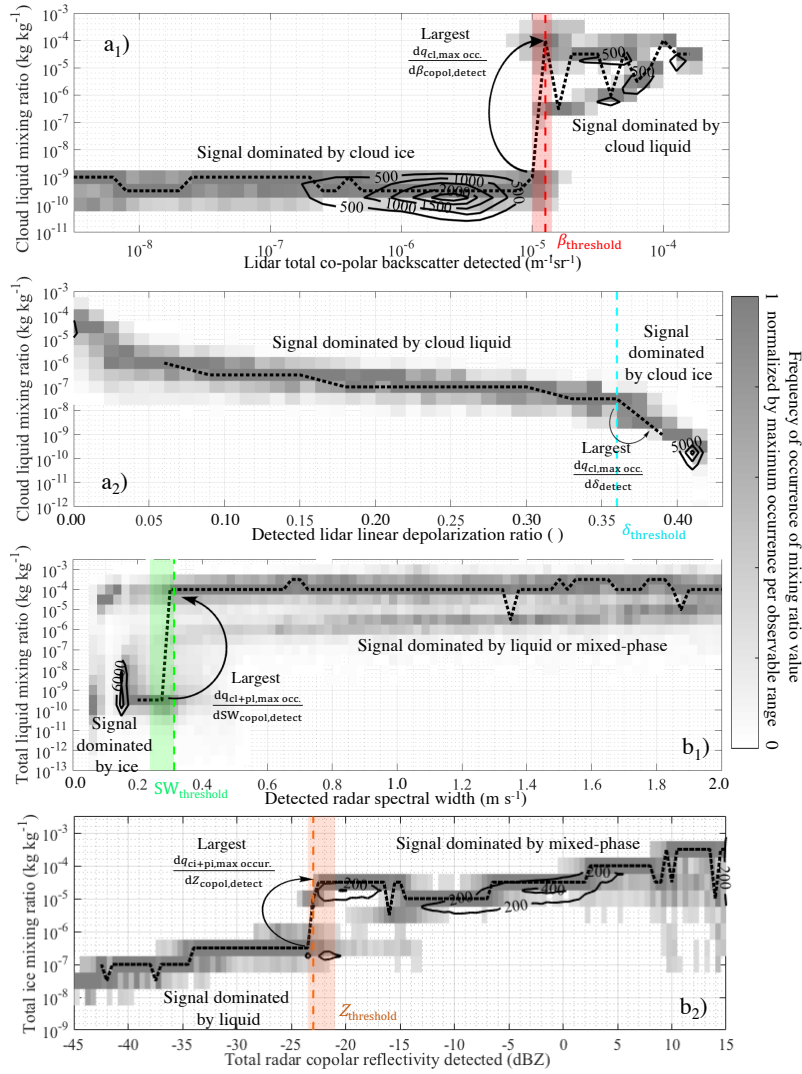
556 557 **6.1 Observational Thresholds for Hydrometeor Phase Identification**

558
559 While the thresholds used for the radar reflectivity, lidar backscattered power, and lidar
560 depolarization ratio are generally accepted by the remote sensing community, the same cannot be said
561 about the radar Doppler velocity and Doppler spectral width thresholds suggested by Shupe (2007).
562 Because simulated mixing ratios of liquid and ice hydrometeors are known in the (GO)²-SIM framework,
563 the use and choice of all such thresholds for phase classification can be evaluated using joint frequency of
564 occurrence histograms of hydrometeor mixing ratios for a single species and forward-simulated observable
565 values (resulting from all hydrometeor types; Fig. 6). This exercise is repeated for each forward-simulation
566 of the ensemble in order to provide a measure of uncertainty and ensure that the choice of empirical
567 relationship does not affect our conclusions.

568
569 As one example, the joint frequency of occurrence histogram of lidar total co-polar backscattered power
570 ($\beta_{\text{copol,total,detect}}$) and cloud liquid mixing ratio is plotted with the objective of isolating cloud ice particles
571 from cloud water droplets (Fig. 6a₁, black contour lines). Two distinct clusters are evident in the joint
572 histogram in Fig. 6a₁: 1) $\beta_{\text{copol,total,detect}}$ between $10^{-6.7} \text{ m}^{-1}\text{sr}^{-1}$ and $10^{-5.1} \text{ m}^{-1}\text{sr}^{-1}$ for cloud liquid water
573 mixing ratios between $10^{-10.6} \text{ kg kg}^{-1}$ and $10^{-8.8} \text{ kg kg}^{-1}$ which we conclude result primarily from cloud ice
574 particle contributions, and 2) $\beta_{\text{copol,total,detect}}$ between $10^{-4.6} \text{ m}^{-1}\text{sr}^{-1}$ and $10^{-3.8} \text{ m}^{-1}\text{sr}^{-1}$ for cloud liquid water
575 mixing ratios between $10^{-6.4} \text{ kg kg}^{-1}$ and $10^{-4.3} \text{ kg kg}^{-1}$ which we conclude result primarily from cloud liquid
576 droplet contributions. Therefore, a threshold for best distinguishing these two distinct populations should
577 lie somewhere between $10^{-5.1} \text{ m}^{-1}\text{sr}^{-1}$ and $10^{-4.6} \text{ m}^{-1}\text{sr}^{-1}$.

578
579 To objectively determine an appropriate threshold to separate different hydrometeor populations, we start
580 by normalizing the joint histogram of mixing ratio values for fixed ranges of observable values of interest.
581 This normalization is done by assigning a value of 1 to the frequency of occurrence of the most frequently
582 occurring mixing ratio value per observable range. It is then possible to evaluate the change of this most
583 frequently occurring mixing ratio as a function of observable value. The observable value that intersects the
584 largest change in most frequently occurring mixing ratio is then set as the threshold value.

585
586 In the example presented in Fig. 6a₁, the darkest grey shading is indicative of the most frequency occurring
587 cloud liquid mixing ratio for each lidar backscattered power range. The dotted black line in Fig. 6a₁
588 connects these most frequently occurring mixing ratio values. A curved arrow points to the largest change
589 in most frequently occurring mixing ratio as a function of $\beta_{\text{copol,total,detect}}$. A red dashed line at $10^{-4.9} \text{ m}^{-1}\text{sr}^{-1}$
590 indicates the lidar backscatter value that intersects this largest change in mixing ratio and represents an
591 objective threshold value for this example forward-simulation. As mentioned earlier, this threshold is
592 expected to change with the choice of empirical relationships used in the forward simulator. For the 576
593 forward-simulator realizations of this version of ModelE outputs, the interquartile range of $\beta_{\text{copol,total,detect}}$
594 threshold values ranged from $10^{-5} \text{ m}^{-1}\text{sr}^{-1}$ to $10^{-4.85} \text{ m}^{-1}\text{sr}^{-1}$ (red shaded vertical column).



596
 597 **Figure 6.** Example of joint frequency of occurrence histograms (contours) and normalized subsets from the
 598 joint histograms (grey shading) for one (GO)²-SIM forward-realization: a₁) $\beta_{\text{copol,total,detect}}$, a₂) δ_{detect} , b₁)
 599 $SW_{\text{copol,detect}}$, and b₂) $Z_{\text{copol,total,detect}}$. These are used for the determination of objective water phase
 600 classifier thresholds (vertical colored dashed lines) that are set at the observational value with the largest
 601 change (see curved arrows) in most frequently occurring mixing ratio. These thresholds are not fixed but
 602 rather re-estimated for each forward-ensemble member. The widths of the color shaded vertical columns
 603 represent the interquartile range spreads generated from 576 different forward-realizations.
 604

605 The different panels in Fig. 6 show that similar observational patterns occur in the water mixing ratio
606 versus lidar or radar observable histograms such that objective thresholds for hydrometeor phase
607 classification can be determined for all of them. The second threshold determined is for the detected lidar
608 linear depolarization (δ_{detect}), once again with the goal of separating returns dominated by cloud droplets
609 versus cloud ice particles (Fig. 6a₂). If we first identify the model grid cells with backscattered power above
610 the lidar detectability threshold of $10^{-6} \text{ m}^{-1} \text{ sr}^{-1}$, the threshold to distinguish between ice particles and liquid
611 droplets is 0.36 (cyan dashed line). In the 576 forward realizations from this version of ModelE this
612 threshold is stable at 0.36. Note that this threshold is not allowed to fall below 0.05 m s^{-1} .
613

614 The third threshold determined is the radar detected co-polar spectral width ($\text{SW}_{\text{copol,detect}}$) value that
615 separates ice dominated from liquid/mixed-phase dominated returns (Fig. 6b₁). We isolate the model grid
616 cells with sub-zero temperatures and look for the most appropriate $\text{SW}_{\text{copol,detect}}$ threshold between 0.2 m s^{-1}
617 and 0.5 m s^{-1} to isolate the ice population. For the example forward-simulation we find a threshold of 0.31
618 m s^{-1} (green dashed line), and over all forward-realizations this threshold ranges from 0.24 m s^{-1} to 0.31 m
619 s^{-1} (green shaded vertical column).
620

621 The last threshold determined is the radar total co-polar reflectivity detected ($Z_{\text{copol,total,detect}}$) value that
622 separates liquid from mixed-phase dominated returns (Fig. 6b₂). If we isolate the model grid cells with sub-
623 zero temperatures, spectral widths within the liquid/mixed-phase range, and with mean Doppler velocities
624 smaller than 1 m s^{-1} , the threshold to distinguish between liquid and mixed-phase is objectively set to -23
625 dBZ (orange dashed line). This threshold ranges from -23.5 dBZ to -21.0 dBZ over the 576 forward
626 realizations obtained from this version of ModelE outputs (orange shaded vertical column).
627

628 The objectively determined thresholds, based on model output mixing ratios, optimize the performance of
629 the hydrometeor phase classification algorithm and are expected to generate the best (by minimizing false
630 detection) hydrometeor phase classifications. Results using these objective flexible thresholds are
631 compared in Sec. 6.4 to results using the fixed empirical thresholds of Shupe (2007).
632

633 6.2 Hydrometeor Phase Map Generation

634
635 Hydrometeor phase maps are produced for each forward realization by applying the objectively
636 determined flexible thresholds or fixed empirical thresholds modified from Shupe (2007) as illustrated in
637 Fig. 7.
638

639 Thresholds are applied in sequence. Where the lidar signal is detected it is used for initial classification of
640 liquid-dominated grid cells (Fig. 7.1, red box) and final classification of ice-dominated grid cells (Fig. 7.1,
641 cyan box). Grid cells initially classified as containing liquid drops by the lidar are subsequently reclassified
642 as either liquid dominated (Fig. 7.2, orange box) or mixed-phase (Fig. 7.2, outside of orange box) by the
643 radar which is more sensitive to the larger ice particles. Because studies suggest that supercooled water
644 layers extend to the tops of shallow clouds, if liquid containing grid cells were identified within 750 m of
645 cloud top, the radar is used to determine if there are other liquid or mixed-phase hydrometeor populations
646 from the range of lidar attenuation to cloud top (Fig.7.2; and just as in Shupe (2007)). Hydrometeor-
647 containing grid cells either not detected by the lidar or whose initial phase classification is inconclusive
648 (Fig. 7.1, inconclusive region) are subsequently classified using their radar moments. If radar spectral width
649 is above the threshold grid cells are finally classified as liquid (Fig.7.3, orange box) or mixed-phase (Fig.
650 7.3, outside the orange box) depending on their other radar moments. If radar spectral width is below the
651 threshold grid cells are finally classified as ice phase (Fig. 7.4). As a final step detected hydrometeors in
652 grid cells at temperatures above $0 \text{ }^\circ\text{C}$ are reclassified to liquid phase while those at temperatures below -40
653 $^\circ\text{C}$ are reclassified to the ice phase.
654

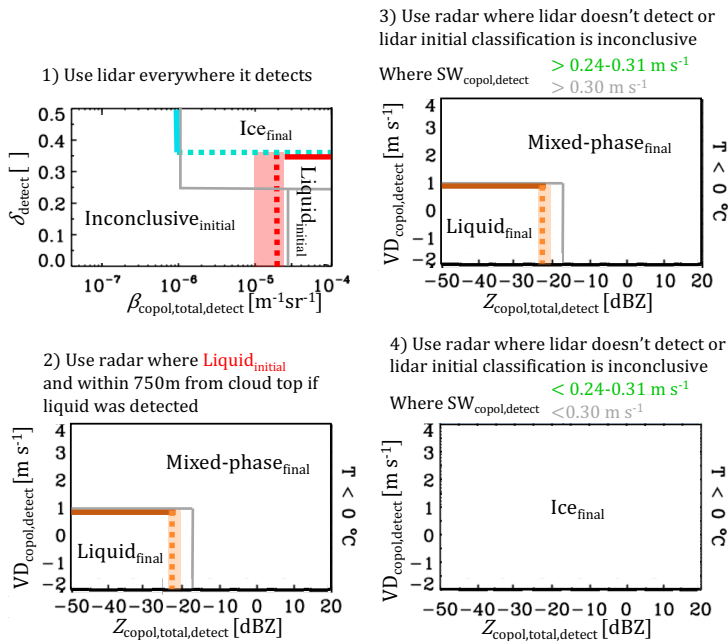
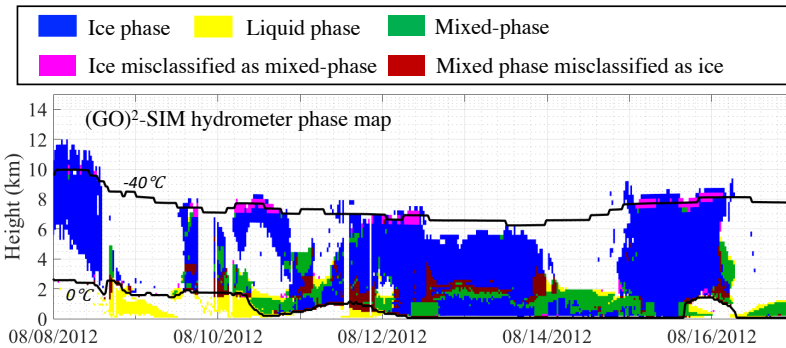
656
657
658
659
660
661
662

Figure 7. Collective illustration of hydrometeor phase classification thresholds and phase classification sequence. Fixed empirical thresholds modified from Shupe (2007) are displayed as grey lines. The objectively determined flexible thresholds are displayed using dashed colored lines and colored shading as in Fig. 6. Note that positive velocities indicate downward motion.

663
664
665
666
667
668
669
670
671
672
673
674
675
676
677
678
679
680

Figure 8 shows an example of $(GO)^2$ -SIM water phase classification for one forward-ensemble member using objectively determined thresholds. During the first day of this example simulation, ModelE produced what appears to be a thick cirrus. The simulator classified this cirrus as mostly ice phase (blue). The following day of 08/09, ModelE generated enough hydrometeors to attenuate both the forward-simulated lidar and radar signals. The algorithm identified these hydrometeors as liquid phase (yellow). For the following few days (08/11-08/14) deep hydrometeor systems extending from the surface to about 8 km were produced. According to $(GO)^2$ -SIM they were mostly made up of ice-phase particles (blue) with two to three shallow mixed-phase layers at 2 km, 4 km and 7 km. Finally, on 08/14 hydrometeor systems appear to become shallower (2-km altitudes) and liquid topped (yellow). For the entire one-year simulation, of the 333,927 detectable hydrometeor-containing grid cells, the phase classifier applied to our example forward-simulation ensemble member identified 12.2 % pure-liquid, 68.7 % pure-ice and 19.1 % mixed-phase conditions. Hydrometeor phase statistics estimated using this objective definition of hydrometeor phase differ by up to 60 % from those discussed at the beginning of this section that were simply based on model output nonzero mixing ratios. This indicates that a large number of grid cells containing detectable hydrometeor populations were dominated by one species and that the amounts of the other species were too small to create a phase classification signal. This highlights the need to create a framework that both objectively identifies grid cells containing detectable hydrometeors populations and determines the phase of the hydrometeors dominating them using a phase classification technique consistent with observations.



681
682
683
684
685
686
687
688
689
690
691

Figure 8. Example output from (GO)²-SIM phase-classification algorithms (using objectively determined thresholds and one set of empirical relationships in the forward-simulator). The locations of ice-phase hydrometeors (blue), liquid-phase hydrometeors (yellow) and mixed-phase hydrometeors (green) are illustrated. After evaluation against the original ModelE output mixing-ratios, we found that some mixed-phase hydrometeors were misclassified as ice phase (red) and some ice-phase hydrometeors were misclassified as mixed phase (magenta). Also indicated are the locations of the 0 °C and -40 °C isotherms (black lines).

6.3 Phase Classification Algorithm Limitations

692
693
694
695
696
697

Hydrometer-phase classification evaluation is facilitated in the context of forward-simulators because inputs (i.e., model-defined hydrometer phase) are known. Model mixing-ratios are used to check for incorrect hydrometer phase classifications over the entire forward-realization ensemble (Table 1b).

698
699
700
701
702
703
704
705
706
707
708

Without any ambiguity, it is possible to identify false-positive phase classifications (Table 1b). A false-positive phase classification occurs when a grid cell containing 0 kg kg⁻¹ of ice particles (liquid drops) is wrongly classified as ice or mixed phase (liquid or mixed phase). In this study a negligible number (0.5 %) of hydrometer-containing model grid cells are wrongly classified as containing liquid. Similarly, a negligible number (~0.0 %) of hydrometer-containing model grid cells are wrongly classified as containing ice particles, whereas 1.1 % of pure liquid- or ice-containing model grid cells are wrongly classified as mixed-phase. Using model mixing ratios, it is possible to determine the appropriate phase of these false-positive classifications (“False negative” row in Table 1b). An additional 1.5 % of all hydrometer-containing model grid cells should be classified as ice phase while a negligible number (0.2 %) of liquid water is missed.

709
710
711
712
713
714
715
716

Quantifying the number of mixed-phase false negatives (i.e., the number of grid cells that should have been, but were not, classified as mixed-phase) is not as straightforward because it requires us to define mixed-phase conditions in model space. For a rough estimate of mixed-phase false negatives we check if model grid cells classified as containing a single phase contained large amounts of hydrometeors of other phase types, with large amount being defined here as a mixing-ratio greater than 10⁻⁵ kg kg⁻¹. This mixing-ratio amount was chosen because it is associated with noticeable changes in observables, as seen in Fig. 6. Using this mixed-phase definition, we find that 1.4 % of liquid-only classified grid cells contained large amounts of ice particles and 3.8 % of ice-only classified grid cells contained large amounts of liquid

717 (“Questionable” row in Table 1b). Everything considered, only 6.9 % of model grid cells with detectable
718 hydrometeor populations were misclassified according to their phase.

719

720 For completeness we examined the circumstances associated with the most frequent phase-classification
721 errors. Most of these errors occurred above the altitude at which the lidar beam was completely attenuated,
722 where only radar spectral widths are used to separate liquid/mixed-phase hydrometeors from ice-phase
723 hydrometeors.

724

725 The first set of phase-classifier errors was a scarcity of pure ice particles (1.5 % false-negative ice phase).
726 In the current (GO)²-SIM implementation, ice particle populations are sometimes incorrectly classified as
727 liquid/mixed-phase populations where cloud ice and precipitating ice hydrometeors coexist. This happens
728 because mixtures of cloud and precipitating ice particles sometimes generate large Doppler spectral widths
729 similar to those of mixed-phase clouds (Fig. 5b₆). In this example simulation ModelE produced such
730 mixtures close to the -40 °C isotherm near the tops of deep cloud systems (e.g., Fig. 8, 08/15 around 8 km;
731 magenta).

732

733 In contrast, mixed-phase conditions were sometimes misclassified as pure ice (3.8 %; “Questionable” row
734 in Table 1b). This occurred when large amounts of liquid drops coexisted with small amounts of ice
735 particles that generated small spectral widths incorrectly associated with pure ice particles (Fig. 5a₅). In this
736 example simulation, ModelE produced such conditions just above the altitude of lidar beam extinction in
737 cloud layers with ice falling into supercooled water layers (e.g., Fig. 8, 08/13 around 3 km; red).

738

739 Other possible misclassification scenarios associated with spectral width retrievals are presented in Fig. 5
740 and identified with the red X-marks. These other misclassification scenarios are not responsible for large
741 misclassification errors here but could be in other simulations. As such, (GO)²-SIM errors should be
742 quantified every time it is applied to a new region or numerical model.

743

744 6.4 Sensitivity on the Choice of Threshold

745

746 The performance of the objectively determined flexible phase-classification thresholds (illustrated
747 using colored dashed lines and shading in Fig. 7) is examined against those empirically derived by Shupe
748 (2007) with one exception (illustrated using grey lines in Fig. 7). The modification to Shupe (2007) is that
749 radar reflectivity larger than 5 dBZ are not associated with the snow category since introducing this
750 assumption was found to increase hydrometeor-phase misclassification (not shown). From Fig. 7 it is
751 apparent that both sets of thresholds are very similar. We estimate that hydrometeor phase frequency of
752 occurrence produced by both threshold sets are within 6.1 % of each other and that the fixed empirical
753 thresholds modified from Shupe (2007) only produce phase misclassification in an additional 0.7 % of
754 hydrometeor-containing grid cells (compare Table 1b to Table 1c). These results suggest that the use of
755 lidar-radar threshold-based techniques for hydrometeor-phase classification depends little on the choice of
756 thresholds.

757

758 7 An Ensemble Approach for [Uncertainty Assessment](#)

759

760 Owing to the limited information content in models with regard to detailed particle property
761 information, all forward simulators must rely on a set of assumptions to estimate hydrometeor
762 backscattered power. (GO)²-SIM performs an uncertainty assessment by performing an ensemble of 576
763 forward simulations based on 18 different empirical relationships (relationships are listed in Table 2).
764 While the relationships used do not cover the entire range of possible backscattering assumptions, they
765 represent an attempt at [uncertainty assessment](#) and illustrate a framework for doing so. We express the
766 spread generated by the different empirical relationships combinations using median values and

Deleted: Uncertainty Quantification

Deleted: uncertainty quantification

769 interquartile ranges (IQR; Table 1b,c). The fact that the largest interquartile range is 3.7 % suggests that the
770 number of grid cells containing detectable hydrometeors as well as hydrometeor phase statistics estimated
771 using the proposed lidar-radar algorithm are rather independent of backscattered power assumptions in the
772 forward simulator. Nevertheless, we suggest using the full range of frequency of occurrences presented in
773 Tables 1b,c for future model evaluation using observations and acknowledge that additional uncertainty is
774 most likely present.

775

776 8 Summary and Conclusions

777

778 Ground-based active remote sensors offer a favorable perspective for the study of shallow and
779 multi-layer mixed-phase clouds because ground-based sensors are able to collect high resolution
780 observations close to the surface where supercooled water layers are expected to be found. In addition,
781 ground-based sensors have the unique capability to collect Doppler velocity information that has the
782 potential to help identify mixed-phase conditions even in multi-layer cloud systems.

783

784 Because of differences in hydrometeor and phase definitions, among other things, observations remain
785 incomplete benchmarks for general circulation model (GCM) evaluation. Here, a GCM-oriented ground-
786 based observation forward-simulator [(GO)²-SIM] framework for hydrometeor-phase evaluation is
787 presented. This framework bridges the gap between observations and GCMs by mimicking observations
788 and their limitations and producing hydrometeor-phase maps with comparable hydrometeor definitions and
789 uncertainties.

790

791 Here, results over the North Slope of Alaska extracted from a one-year global ModelE (current
792 development version) simulation are used as an example. (GO)²-SIM uses as input native resolution GCM
793 grid-average hydrometeor (cloud and precipitation, liquid and ice) area fractions, mixing ratios, mass-
794 weighted fall speeds and effective radii. These variables offer a balance between those most essential for
795 forward simulation of observed hydrometeor backscattering and those likely to be available from a range of
796 GCMs, making (GO)²-SIM a portable tool for model evaluation. (GO)²-SIM outputs statistics from 576
797 forward-simulation ensemble members all based on a different combination of eighteen empirical
798 relationships that relate simulated water content to hydrometeor backscattered power as would be observed
799 by vertically pointing micropulse lidar and Ka-band radar; The interquartile range of these statistics being
800 used as an uncertainty measure.

801

802 (GO)²-SIM objectively determines which hydrometeor-containing model grid cells can be assessed based
803 on sensor capabilities, bypassing the need to arbitrarily filter trace amounts of simulated hydrometeor
804 mixing ratios that may be unphysical or just numerical noise. Limitations that affect sensor capabilities
805 represented in (GO)²-SIM include attenuation and range dependent sensitivity. In this approach 78.3 % of
806 simulated grid cells containing nonzero hydrometeor mixing ratios were detectable and can be evaluated
807 using real observations, with the rest falling below the detection capability of the forward-simulated lidar
808 and radar leaving them unevaluated. This shows that comparing all hydrometeors produced by models with
809 those detected by sensors would lead to inconsistencies in the evaluation of quantities as simple as cloud
810 and precipitation locations and fraction.

811

812 While information can be gained from comparing the forward-simulated and observed fields, hydrometeor-
813 phase evaluation remains challenging owing to inconsistencies in hydrometeor-phase definitions. Models
814 evolve ice and liquid water species separately such that their frequency of occurrence can easily be
815 estimated. However, sensors record information from all hydrometeor species within a grid cell without
816 distinction between signals originating from ice particles or liquid drops. The additional observables of
817 lidar linear depolarization ratio and radar mean Doppler velocity and spectral width are forward simulated
818 to retrieve hydrometeor phase. The results presented here strengthen the idea that hydrometeor-phase

Deleted: going forward,

820 characteristics lead to distinct signatures in lidar and radar observables, including the radar Doppler
821 moments which have not been evaluated previously. Our analysis confirms that distinct patterns in
822 observational space are related to hydrometeor phase and an objective technique to isolate liquid, mixed-
823 phase and ice conditions using simulated hydrometeor mixing ratios was presented. The thresholds
824 produced by this technique are close to those previously estimated using real observations, further
825 highlighting the robustness of thresholds for hydrometeor-phase classification.

826
827 The algorithm led to hydrometeor phase misclassification in no more than 6.9 % of the hydrometeor-
828 containing grid cells. Its main limitations were confined above the altitude of lidar total attenuation where it
829 sometimes failed to identify additional mixed-phase layers dominated by liquid water drops and with few
830 ice particles. Using the same hydrometeor-phase definition for forward-simulated observables and real
831 observations should produce hydrometeor-phase statistics with comparable uncertainties. Alternatively,
832 disregarding how hydrometeor phase is observationally retrieved would lead to discrepancies in
833 hydrometeor-phase frequency of occurrence up to 40 %, a difference attributable to methodological bias
834 and not to model error. So, while not equivalent to model “reality” a forward-simulator framework offers
835 the opportunity to compare simulated and observed hydrometeor-phase maps with similar limitations and
836 uncertainties for a fair model evaluation.

837
838 The next steps to GCM evaluation using ground-based observations include the creation of an artifact-free
839 observational benchmark and addressing model and observation scale differences. While the (GO)²-SIM
840 modules presented here capture sensor limitations related to backscattered power attenuations, they do not
841 account for sensitivity inconsistencies, clutter and insect contamination, all of which affect the observations
842 collected by the real sensors. Only thorough evaluation of observational datasets and application of
843 masking algorithms to them can remediate these issues. Several approaches, from the subsampling of
844 GCMs to the creation of [reflectivity contoured frequency by altitude diagrams \(CFADs\)](#), have been
845 proposed to address the scale difference. A follow-up study will describe an approach by which vertical and
846 temporal resampling of observations can help reduce the scale gap. Furthermore, it will be showed that,
847 using simplified model evaluation targets based on three atmospheric regions separated by constant
848 pressure levels, ground-based observations can be used for GCM hydrometeor-phase evaluation.

849
850 (GO)²-SIM is a step towards creating a fair hydrometeor-phase comparison between GCM output and
851 ground-based observations. Owing to its simplicity and robustness, (GO)²-SIM is expected to help assist in
852 model evaluation and development for models such as ModelE, specifically with respect to hydrometeor
853 phase in shallow cloud systems.

854 855 **Code Availability**

856
857 Results here are based on ModelE tag modelE3_2017-06-14, which is not a publicly released
858 version of ModelE but is available on the ModelE developer repository
859 at https://simplex.giss.nasa.gov/cgi-bin/gitweb.cgi?p=modelE.git;a=tag;h=refs/tags/modelE3_2017-06-14.
860 The (GO)²-SIM modules described in the current manuscript can be fully reproduced using the information
861 provided. Interested parties are encouraged to contact the corresponding author for additional information
862 on how to interface their numerical model with (GO)²-SIM.

863 864 **Acknowledgements**

865
866 K. Lamer and E. Clothiaux’s contributions to this research were funded by subcontract 300324 of
867 the Pennsylvania State University with the Brookhaven National Laboratory in support to the ARM-ASR
868 Radar Science group. The contributions of A. Fridlind, A. Ackerman, and M. Kelley were partially
869 supported by the Office of Science (BER), U.S. Department of Energy, under agreement DE-SC0016237,

870 the NASA Radiation Sciences Program, and the NASA Modeling, Analysis and Prediction Program.
871 Resources supporting this work were provided by the NASA High-End Computing (HEC) Program
872 through the NASA Center for Climate Simulation (NCCS) at Goddard Space Flight Center. [Finally, the](#)
873 [authors would like to thank the two anonymous reviewers and the editor of this manuscript for their](#)
874 [comments](#).

Deleted: ¶

876 References

- 877 Atlas, D.: The estimation of cloud parameters by radar, *J. Meteorol.*, 11, 309-317, 1954.
- 879 Atlas, D., Matrosov, S. Y., Heymsfield, A. J., Chou, M.-D., and Wolff, D. B.: Radar and radiation
880 properties of ice clouds, *J. Appl. Meteorol.*, 34, 2329-2345, 1995.
- 881 Battaglia, A., and Delanoë, J.: Synergies and complementarities of CloudSat-CALIPSO snow
882 observations, *J. Geophys. Res.: Atmos.*, 118, 721-731, 2013.
- 883 Battan, L. J.: Radar observation of the atmosphere, University of Chicago, Chicago, Illinois, 1973.
- 884 Bodas-Salcedo, A., Webb, M., Bony, S., Chepfer, H., Dufresne, J.-L., Klein, S., Zhang, Y.,
885 Marchand, R., Haynes, J., and Pincus, R.: COSP: Satellite simulation software for model assessment, *Bull.*
886 *Amer. Meteorol. Soc.*, 92, 1023-1043, 2011.
- 887 Bretherton, C. S., and Park, S.: A new moist turbulence parameterization in the Community
888 Atmosphere Model, *J. Climate*, 22, 3422-3448, 2009.
- 889 Cesana, G., and Chepfer, H.: Evaluation of the cloud thermodynamic phase in a climate model
890 using CALIPSO-GOCCP, *J. Geophys. Res.: Atmos.*, 118, 7922-7937, 2013.
- 891 Chepfer, H., Bony, S., Winker, D., Chiriaco, M., Dufresne, J. L., and Sèze, G.: Use of CALIPSO
892 lidar observations to evaluate the cloudiness simulated by a climate model, *Geophys. Res. Lett.*, 35, 2008.
- 893 de Boer, G., Eloranta, E. W., and Shupe, M. D.: Arctic mixed-phase stratiform cloud properties
894 from multiple years of surface-based measurements at two high-latitude locations, *J. Atmos. Sci.*, 66, 2874-
895 2887, 2009.
- 896 Dong, X., and Mace, G. G.: Arctic stratus cloud properties and radiative forcing derived from
897 ground-based data collected at Barrow, Alaska, *J. climate*, 16, 445-461, 2003.
- 898 Ellis, S. M., and Vivekanandan, J.: Liquid water content estimates using simultaneous S and Ka
899 band radar measurements, *Radio Science*, 46, 2011.
- 900 English, J. M., Kay, J. E., Gettelman, A., Liu, X., Wang, Y., Zhang, Y., and Chepfer, H.:
901 Contributions of clouds, surface albedos, and mixed-phase ice nucleation schemes to Arctic radiation biases
902 in CAM5, *J. Climate*, 27, 5174-5197, 2014.
- 904 Everitt, B., and Hand, D.: Mixtures of normal distributions, in: *Finite Mixture Distributions*,
905 Springer, 25-57, 1981.
- 906 Fox, N. I., and Illingworth, A. J.: The retrieval of stratocumulus cloud properties by ground-based
907 cloud radar, *J. Appl. Meteorol.*, 36, 485-492, 1997.
- 908

910 Frey, W., Maroon, E., Pendergrass, A., and Kay, J.: Do Southern Ocean Cloud Feedbacks Matter
911 for 21st Century Warming?, *Geophys. Res. Lett.*, 2017.

912 Gettelman, A., and Morrison, H.: Advanced two-moment bulk microphysics for global models. Part
913 I: Off-line tests and comparison with other schemes, *J. Climate*, 28, 1268-1287, 2015.

914 Gettelman, A., Morrison, H., Santos, S., Bogenschutz, P., and Caldwell, P.: Advanced two-moment
915 bulk microphysics for global models. Part II: Global model solutions and aerosol–cloud interactions, *J.*
916 *Climate*, 28, 1288-1307, 2015.

917 Hagen, M., and Yuter, S. E.: Relations between radar reflectivity, liquid-water content, and rainfall
918 rate during the MAP SOP, *Quart. J. Roy. Meteorol. Soc.*, 129, 477-493, 2003.

919 Haynes, J., Luo, Z., Stephens, G., Marchand, R., and Bodas-Salcedo, A.: A multipurpose radar
920 simulation package: QuickBeam, *Bull. Amer. Meteorol. Soc.*, 88, 1723-1727, 2007.

921 Heymsfield, A., Winker, D., Avery, M., Vaughan, M., Diskin, G., Deng, M., Mitev, V., and
922 Matthey, R.: Relationships between ice water content and volume extinction coefficient from in situ
923 observations for temperatures from 0 to -86° C: Implications for spaceborne lidar retrievals, *J. Appl.*
924 *Meteorol. Climatol.*, 53, 479-505, 2014.

925 Heymsfield, A. J., Winker, D., and van Zadelhoff, G. J.: Extinction-ice water content-effective
926 radius algorithms for CALIPSO, *Geophys. Res. Lett.*, 32, 2005.

927 Hogan, R. J., Illingworth, A., O'Connor, E., and Baptista, J.: Characteristics of mixed-phase clouds.
928 II: A climatology from ground-based lidar, *Quart. J. Roy. Meteorol. Soc.*, 129, 2117-2134, 2003.

929 Hogan, R. J., Behera, M. D., O'Connor, E. J., and Illingworth, A. J.: Estimate of the global
930 distribution of stratiform supercooled liquid water clouds using the LITE lidar, *Geophys. Res. Lett.*, 31,
931 2004.

932 Hogan, R. J., and O'Connor, E.: Facilitating cloud radar and lidar algorithms: The Cloudnet
933 Instrument Synergy/Target Categorization product, Cloudnet documentation, 2004.

934 Hogan, R. J., Mittermaier, M. P., and Illingworth, A. J.: The retrieval of ice water content from
935 radar reflectivity factor and temperature and its use in evaluating a mesoscale model, *J. Appl. Meteorol.*
936 *Climatol.*, 45, 301-317, 2006.

937 Hu, Y., Vaughan, M., Liu, Z., Lin, B., Yang, P., Flittner, D., Hunt, B., Kuehn, R., Huang, J., and
938 Wu, D.: The depolarization-attenuated backscatter relation: CALIPSO lidar measurements vs. theory,
939 *Optics Express*, 15, 5327-5332, 2007a.

940 Hu, Y., Vaughan, M., McClain, C., Behrenfeld, M., Maring, H., Anderson, D., Sun-Mack, S.,
941 Flittner, D., Huang, J., Wielicki, B., Minnis, P., Weimer, C., Trepte, C., and Kuehn, R.: Global statistics of
942 liquid water content and effective number concentration of water clouds over ocean derived from
943 combined CALIPSO and MODIS measurements, *Atmos. Chem. Phys.*, 7, 3353-3359, 10.5194/acp-7-
944 3353-2007, 2007b.

945 Hu, Y., Winker, D., Vaughan, M., Lin, B., Omar, A., Trepte, C., Flittner, D., Yang, P., Nasiri, S. L.,
946 and Baum, B.: CALIPSO/CALIOP cloud phase discrimination algorithm, *J. Atmos. Ocean. Technol.*, 26,
947 2293-2309, 2009.

948 Hu, Y., Rodier, S., Xu, K. m., Sun, W., Huang, J., Lin, B., Zhai, P., and Josset, D.: Occurrence,
949 liquid water content, and fraction of supercooled water clouds from combined CALIOP/IIR/MODIS
950 measurements, *J. Geophys. Res.: Atmos.*, 115, 2010.

951 Huang, Y., Siems, S. T., Manton, M. J., Hande, L. B., and Haynes, J. M.: The structure of low-
952 altitude clouds over the Southern Ocean as seen by CloudSat, *J. Climate*, 25, 2535-2546, 2012a.

953 Huang, Y., Siems, S. T., Manton, M. J., Protat, A., and Delanoë, J.: A study on the low-altitude
954 clouds over the Southern Ocean using the DARDAR-MASK, *J. Geophys. Res.: Atmos.*, 117, 2012b.

955 Intrieri, J., Shupe, M., Uttal, T., and McCarty, B.: An annual cycle of Arctic cloud characteristics
956 observed by radar and lidar at SHEBA, *J. Geophys. Res.: Oceans*, 107, 2002.

957 Kalesse, H., Szyrmer, W., Kneifel, S., Kollias, P., and Luke, E.: Fingerprints of a riming event on
958 cloud radar Doppler spectra: observations and modeling, *Atmos. Chem. Phys.*, 16, 2997-3012, 2016.

959 Kay, J. E., Bourdages, L., Miller, N. B., Morrison, A., Yettella, V., Chepfer, H., and Eaton, B.:
960 Evaluating and improving cloud phase in the Community Atmosphere Model version 5 using spaceborne
961 lidar observations, *J. Geophys. Res.: Atmos.*, 121, 4162-4176, 2016.

962 Kikuchi, K., Tsuboya, S., Sato, N., Asuma, Y., Takeda, T., and Fujiyoshi, Y.: Observation of
963 wintertime clouds and precipitation in the Arctic Canada (POLEX-North), *J. Meteorol. Soc. Japan. Ser. II*,
964 60, 1215-1226, 1982.

965 Klein, S. A., McCoy, R. B., Morrison, H., Ackerman, A. S., Avramov, A., Boer, G. d., Chen, M.,
966 Cole, J. N., Del Genio, A. D., and Falk, M.: Intercomparison of model simulations of mixed-phase clouds
967 observed during the ARM Mixed-Phase Arctic Cloud Experiment. I: Single-layer cloud, *Quart. J. Roy.
968 Meteorol. Soc.*, 135, 979-1002, 2009.

969 Kollias, P., Miller, M. A., Luke, E. P., Johnson, K. L., Clothiaux, E. E., Moran, K. P., Widener, K.
970 B., and Albrecht, B. A.: The Atmospheric Radiation Measurement Program cloud profiling radars: Second-
971 generation sampling strategies, processing, and cloud data products, *J. Atmos. Ocean. Technol.*, 24, 1199-
972 1214, 2007.

973 Kollias, P., Rémillard, J., Luke, E., and Szyrmer, W.: Cloud radar Doppler spectra in drizzling
974 stratiform clouds: 1. Forward modeling and remote sensing applications, *J. Geophys. Res.: Atmos.*, 116,
975 2011.

976 Kollias, P., Clothiaux, E. E., Ackerman, T. P., Albrecht, B. A., Widener, K. B., Moran, K. P., Luke,
977 E. P., Johnson, K. L., Bharadwaj, N., and Mead, J. B.: Development and applications of ARM millimeter-
978 wavelength cloud radars, *Meteorological Monographs*, 57, 17.11-17.19, 2016.

979 Kuehn, R., Holz, R., Eloranta, E., Vaughan, M., and Hair, J.: Developing a Climatology of Cirrus
980 Lidar Ratios Using University of Wisconsin HSRL Observations, *EPJ Web of Conferences*, 2016, 16009,

981 Liao, L., and Sassen, K.: Investigation of relationships between Ka-band radar reflectivity and ice
982 and liquid water contents, *Atmospheric Res.*, 34, 231-248, 1994.

983 Liu, C.-L., and Illingworth, A. J.: Toward more accurate retrievals of ice water content from radar
984 measurements of clouds, *J. Appl. Meteorol.*, 39, 1130-1146, 2000.

985 McCoy, D. T., Tan, I., Hartmann, D. L., Zelinka, M. D., and Storelvmo, T.: On the relationships
986 among cloud cover, mixed-phase partitioning, and planetary albedo in GCMs, *J. Advances in Modeling*
987 *Earth Systems*, 8, 650-668, 2016.

988 O'Connor, E. J., Illingworth, A. J., and Hogan, R. J.: A technique for autocalibration of cloud lidar,
989 *J. Atmos. Ocean. Technol.*, 21, 777-786, 2004.

990 Rémillard, J., and Tselioudis, G.: Cloud regime variability over the Azores and its application to
991 climate model evaluation, *J. Climate*, 28, 9707-9720, 2015.

992 Sassen, K.: Ice cloud content from radar reflectivity, *J. climate and Appl. Meteorol.*, 26, 1050-1053,
993 1987.

994 Sassen, K.: The polarization lidar technique for cloud research: A review and current assessment,
995 *Bull. Amer. Meteorol. Soc.*, 72, 1848-1866, 1991.

996 Sato, N., Kikuchi, K., Barnard, S. C., and Hogan, A. W.: Some characteristic properties of ice
997 crystal precipitation in the summer season at South Pole Station, Antarctica, *J. Meteorol. Soc. Japan. Ser.*
998 *II*, 59, 772-780, 1981.

999 Sauvageot, H., and Omar, J.: Radar reflectivity of cumulus clouds, *J. Atmos. Ocean. Technol.*, 4,
1000 264-272, 1987.

1001 Schmidt, G. A., Kelley, M., Nazarenko, L., Ruedy, R., Russell, G. L., Aleinov, I., Bauer, M., Bauer,
1002 S. E., Bhat, M. K., and Bleck, R.: Configuration and assessment of the GISS ModelE2 contributions to the
1003 CMIP5 archive, *J. Adv. Model. Earth Syst.*, 6, 141-184, 2014.

1004 Sekhon, R. S., and Srivastava, R.: Doppler radar observations of drop-size distributions in a
1005 thunderstorm, *J. Atmos. Sci.*, 28, 983-994, 1971.

1006 Shupe, M. D.: A ground-based multisensor cloud phase classifier, *Geophys. Res. Lett.*, 34, 2007.

1007 Tan, I., and Storelvmo, T.: Sensitivity study on the influence of cloud microphysical parameters on
1008 mixed-phase cloud thermodynamic phase partitioning in CAM5, *J. Atmos. Sci.*, 73, 709-728, 2016.

1009 Tan, I., Storelvmo, T., and Zelinka, M. D.: Observational constraints on mixed-phase clouds imply
1010 higher climate sensitivity, *Science*, 352, 224-227, 2016.

1011 Tatarevic, A., and Kollias, P.: User's Guide to Cloud Resolving Model Radar Simulator (CR-SIM),
1012 McGill University Clouds Research Group, Document available at [http://radarscience.weebly.com/radar-](http://radarscience.weebly.com/radar-simulators.html)
1013 [simulators.html](http://radarscience.weebly.com/radar-simulators.html). 2015.

1014 Winker, D. M.: Accounting for multiple scattering in retrievals from space lidar. Proceedings
1015 Volume 5059, 12th International Workshop on Lidar Multiple Scattering
1016 Experiments; <https://doi.org/10.1117/12.512352>, 2003
1017

1018 Yoshida, R., Okamoto, H., Hagihara, Y., and Ishimoto, H.: Global analysis of cloud phase and ice
1019 crystal orientation from Cloud-Aerosol Lidar and Infrared Pathfinder Satellite Observation (CALIPSO)
1020 data using attenuated backscattering and depolarization ratio, *J. Geophys. Res.: Atmos.*, 115, 2010.

l021 Zhang, Y., Xie, S., Klein, S. A., Marchand, R., Kollias, P., Clothiaux, E. E., Lin, W., Johnson, K.,
l022 Swales, D., and Bodas-Salcedo, A.: The ARM Cloud Radar Simulator for Global Climate Models: A New
l023 Tool for Bridging Field Data and Climate Models, Bull. Amer. Meteorol. Soc., 2017.
l024
l025
l026

